

Three-dimensional modeling of the Ca II H and K lines in the solar atmosphere

Johan P. Bjørgen¹, Andrii V. Sukhorukov^{1,2}, Jorrit Leenaarts¹, Mats Carlsson^{3,4}, Jaime de la Cruz Rodríguez¹, Göran B. Scharmer¹, and Viggo H. Hansteen^{3,4}

¹ Institute for Solar Physics, Department of Astronomy, Stockholm University, AlbaNova University Centre, 106 91 Stockholm, Sweden
e-mail: johan.bjorgen@astro.su.se

² Main Astronomical Observatory, National Academy of Sciences of Ukraine, 27 Akademika Zabolotnoho Str., 03680 Kyiv, Ukraine

³ Institute of Theoretical Astrophysics, University of Oslo, PO Box 1029, Blindern, 0315 Oslo, Norway

⁴ Rosseland Centre for Solar Physics, University of Oslo, PO Box 1029, Blindern, 0315 Oslo, Norway

Received 11 September 2017 / Accepted 1 December 2017

ABSTRACT

Context. CHROMIS, a new imaging spectrometer at the Swedish 1-m Solar Telescope (SST), can observe the chromosphere in the H and K lines of Ca II at high spatial and spectral resolution. Accurate modeling as well as an understanding of the formation of these lines are needed to interpret the SST/CHROMIS observations. Such modeling is computationally challenging because these lines are influenced by strong departures from local thermodynamic equilibrium, three-dimensional radiative transfer, and partially coherent resonance scattering of photons.

Aims. We aim to model the Ca II H and K lines in 3D model atmospheres to understand their formation and to investigate their diagnostic potential for probing the chromosphere.

Methods. We model the synthetic spectrum of Ca II using the radiative transfer code Multi3D in three different radiation-magnetohydrodynamic model atmospheres computed with the Bifrost code. We classify synthetic intensity profiles according to their shapes and study how their features are related to the physical properties in the model atmospheres. We investigate whether the synthetic data reproduce the observed spatially-averaged line shapes, center-to-limb variation and compare this data with SST/CHROMIS images.

Results. The spatially-averaged synthetic line profiles show too low central emission peaks, and too small separation between the peaks. The trends of the observed center-to-limb variation of the profiles properties are reproduced by the models. The Ca II H and K line profiles provide a temperature diagnostic of the temperature minimum and the temperature at the formation height of the emission peaks. The Doppler shift of the central depression is an excellent probe of the velocity in the upper chromosphere.

Key words. Sun: chromosphere – methods: numerical – radiative transfer

1. Introduction

The resonance doublet of Ca II represents the two strongest lines in the visible solar spectrum, the H line at 3968.469 Å and the K line at 3933.663 Å; all wavelengths are given in air for $\lambda > 2000$ Å. Observations through the wings and cores of these lines allow us to investigate the photosphere and chromosphere. The H and K lines of Ca II share similar formation properties as the h and k lines of Mg II, typically showing wide damping wings, and central reversals in their cores. As calcium is 18 times less abundant than magnesium in the solar atmosphere (Asplund et al. 2009), the H and K line cores are formed lower in the chromosphere than the h and k cores.

Most of the strongest and diagnostically important chromospheric lines, such as Mg II h and k or H I Ly- α and Ly- β lines, reside in the ultraviolet part of the spectrum that is absorbed by the Earth's atmosphere, and therefore these lines must be observed from space. The Ca II H and K lines are in the violet part of the visible spectrum and can be observed with ground-based facilities such as the Swedish 1-m Solar Telescope (SST;

Scharmer et al. 2003), the German Vacuum Tower Telescope (e.g., Tritschler et al. 2007), GREGOR (Sobotka et al. 2016), and the Dunn Solar Telescope (e.g., Reardon et al. 2009).

The H and K line wings are formed in the photosphere with their opacity following local thermodynamic equilibrium (LTE) (Rutten et al. 2004; Sheminova 2012). They were used to obtain the temperature stratification of the upper photosphere (Roupe van der Voort 2002; Reardon et al. 2009; Henriques 2012) and to investigate the reversed granulation both in observations and simulations (Leenaarts & Wedemeyer-Böhm 2005).

The H and K line cores are formed in the chromosphere and cover a narrow spectral range of ~ 0.4 Å. So far, imaging observations in the cores have been performed with broadband filters with wide transmission profiles 0.3–3 Å (e.g., Zirin 1974; Rutten et al. 2004; Kosugi et al. 2007; Reardon et al. 2009; Pietarila et al. 2009). Thus, previously observed H and K core images were strongly contaminated with photospheric signal coming from the wings.

In August 2016 the new instrument CHROMIS was installed at the SST. The CHROMIS instrument is an imaging spectrometer for the blue part of the spectrum designed as a dual

Fabry–Pérot filter system with a spectral transmission profile of ~ 120 mÅ width around 400 nm. The system is optimized for a short integration time allowing us to scan fast through the line core with a high time cadence and minimal degradation caused by the atmospheric turbulence. By using image post-processing CHROMIS data can reach a diffraction-limited spatial resolution of $1.22\lambda/D \approx 0''.1$ (or 73 km on the surface of the Sun), which is close to the spatial resolution of current magnetohydrodynamic simulations of the chromosphere (Carlsson et al. 2016).

The CHROMIS instrument allows us to sample the inner wings and line core of the H or K lines in ~ 10 s with multiple frames and good signal to noise in two-dimensional (2D) images at the diffraction limit and at a high spectral resolution so that a clean chromospheric signal is obtained.

In the solar spectrum, the infrared triplet of Ca II consists of three strong lines at 8498.018, 8542.089, and 8662.140 Å, whose cores are formed in the chromosphere as well. Among these lines, the Ca II 8542 Å line is the most studied and is used to investigate the magnetic field and temperature structure (see Cauzzi et al. 2008; de la Cruz Rodríguez et al. 2013, and reference therein).

The 8542 Å line is only weakly affected by horizontal radiative transfer (3D) and partial redistribution (PRD) effects and can be modeled with a modest computational effort in one-dimensional (1D) models (de la Cruz Rodríguez et al. 2012).

The H and K lines are formed much higher in the less dense upper chromosphere where 3D and PRD effects play a more essential role in line formation (Miyamoto 1953), than in the infrared triplet of Ca II. Previously, these lines have been modeled including effects of PRD, but only in a one-dimensional (1D) radiative transfer approach (Vardavas & Cram 1974; Shine et al. 1975; Uitenbroek 1989; Solanki et al. 1991; Rezaei et al. 2008). Using a 3D non-LTE radiative transfer approach including effects of PRD has become feasible recently with an upgrade of the Multi3D code (Sukhorukov & Leenaarts 2017). Previously, the most accurate treatment of chromospheric lines was to model features in the core and wings of lines separately using different numerical codes such as in Leenaarts et al. (2013b) or Pereira et al. (2013). The Multi3D code was used to model the line core including 3D radiative transfer but in the simplifying approximation of complete redistribution (CRD). The RH code (Uitenbroek 2001) was used to model the wings of the line using a 1.5D radiative transfer approach but including PRD effects, which are essential in the inner wings.

In this paper, we use various model atmospheres (3D snapshots) computed with the Bifrost code (Gudiksen et al. 2011), to model the formation of the Ca II H and K lines in a full 3D non-LTE PRD approach using the Multi3D code. We compare our calculated data with observations of a quiet Sun region taken by SST/CHROMIS.

Section 2 presents the observations taken with SST/CHROMIS. We discuss the method and the setup of our computations and important details of the PRD line transfer in Sect. 3. We compare morphological properties of images and statistical properties of the line profile features for our calculated and observed data sets in Sect. 5. In Sect. 6, we discuss how the observed features of the lines correlate with the properties of the atmosphere and what observable diagnostics are the most useful to probe the chromosphere. In Sect. 7, we conclude and suggest how observations in the Ca II H and K lines can be used to study the chromosphere.

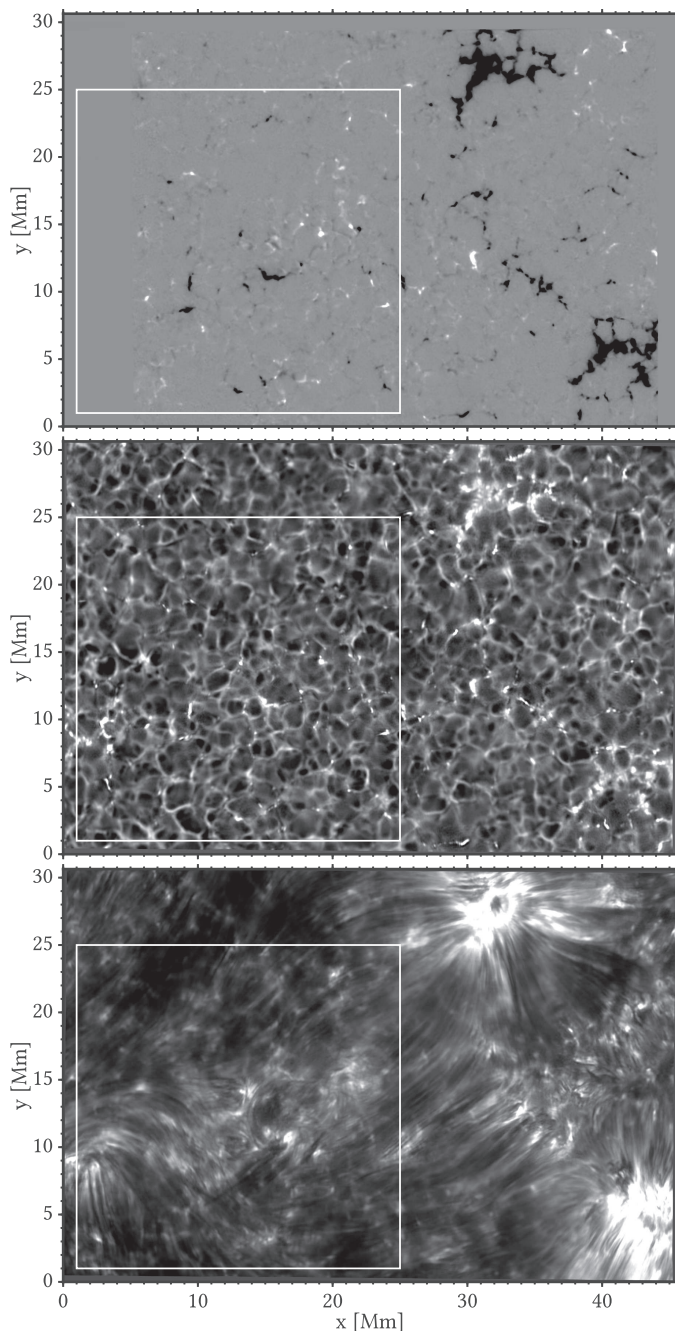


Fig. 1. Magnetogram (*upper panel*) and Ca II K images (*middle panel* and *lower panel*) taken by SST/CHROMIS of the quiet Sun near the disk center ($\mu = 1.0$). *Upper panel*: vertical magnetic field obtained from Milne–Eddington inversion with Fe I taken by SST/CRISP is shown. The color bar range is $[-300, 300]$ G. *Middle panel*: red wing position at $\Delta\lambda = +1409$ mÅ is indicated. *Lower panel*: line center position at $\Delta\lambda = 0$ mÅ is indicated. The white square outlines the region that we compare with our simulations (see Fig. 13).

2. Observations

We used data observed with the CHROMIS instrument at the Swedish 1-m Solar Telescope on October 12, 2016 at 10:46–10:56 UT. The target was a quiet Sun region near the disk center at $\theta_x = 2''$, $\theta_y = -38''$ (helioprojective-Cartesian coordinates).

The Ca II K line was sampled with 36 wavelength points covering a 1.409 Å interval around the line center at 3933.664 Å

with one continuum point at 4000 Å. The line core was sampled within a ± 0.528 Å interval with 59 mÅ spacing. The line wings were sampled outside the core interval up to ± 1.409 Å with 118 mÅ spacing. The camera was run at 80 frames per second with an exposure time of 12 ms; a full line scan took 13 s. The CHROMIS spectrometer has a spectral transmission profile with a 120 mÅ FWHM, a field of view about $63'' \times 42''$ and a pixel size of $0''.0375$.

The Ca II K data set is complemented with observations of the magnetically sensitive Fe I 6302 Å line taken simultaneously on the same target with the CRisp Imaging SpectroPolarimeter (CRISP; Scharmer et al. 2008). The Fe I 6302 Å was sampled with 16 wavelength points on a non-equidistant wavelength grid covering from -1180 to $+80$ mÅ around 6302 Å. A full line scan took 8 s. We acquired also simultaneous CRISP observations in Ca II 8542 Å and H- α , so the total cadence is 37 s.

Final data sets were produced from the raw data using the CHROMISRED pipeline (Löfdahl et al., in prep.) for the Ca II K observations and the CRISPRED pipeline (de la Cruz Rodríguez et al. 2015) for the Fe I observations. The CHROMIS data were calibrated by scaling the spatially averaged spectrum to an atlas profile.

Figure 1 shows two images from Ca II K observations in the red wing and the core of the line. The wing image shows the upper photosphere with a distinct reversed granulation pattern and bright magnetic field concentrations in intergranular lanes. The core image shows the chromosphere covered with thin, elongated fibrils that appear resolved at the spatial resolution of CHROMIS. In the upper panel we show the vertical component of the magnetic field vector derived from a Milne–Eddington inversion of the Fe I photospheric data. These inversions were performed with a modified version of the 1D code presented in Asensio Ramos & de la Cruz Rodríguez (2015).

From the whole field of view we selected a square region of the quiet Sun, which is outlined in Fig. 1. This region matches the physical extent of our simulations and has a similar photospheric magnetic field configuration. We use observed data within this region for comparison with our synthetic data.

3. Modeling

3.1. Radiative transfer computations

We numerically solve the non-LTE radiative transfer problem with the latest version of the Multi3D code (Leenaarts & Carlsson 2009) in various model atmospheres discretized on a Cartesian three-dimensional (3D) grid.

For a given model atom, the code simultaneously solves the system of statistical equilibrium equations and integrates the radiative transfer equation at spectral points covered by the bound-bound and bound-free transitions of the model atom. The solution is computed by iteration until convergence using multilevel accelerated Λ -iteration (M-ALI) with preconditioned radiative rates following Rybicki & Hummer (1991, 1992). The method of short characteristics (Olson & Kunasz 1987) is used to integrate the transfer equation. Either linear or the third-order Hermitian (Auer 2003; Ibgui et al. 2013) interpolation is used to approximate the source function in the formal solution of the transfer equation. We use the 24-angle quadrature (set “A4”) from Carlson (1963).

The code allows us to solve the radiative transfer equation either in 3D by taking into account the horizontal transfer of

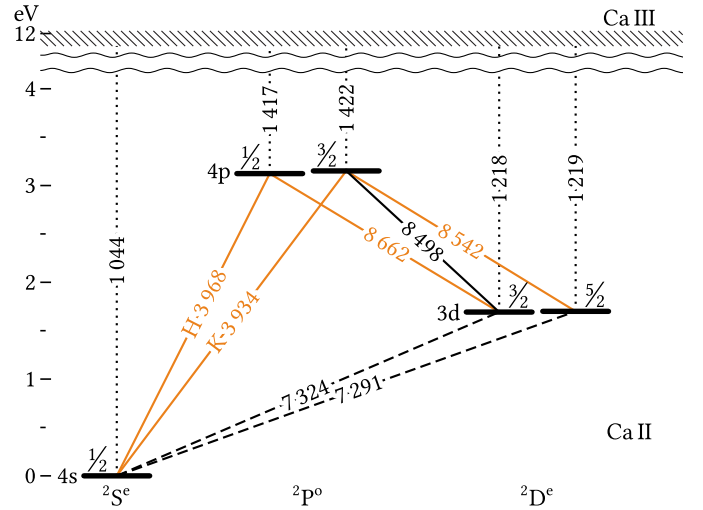


Fig. 2. Term diagram of the Ca II model atom. Atomic levels (horizontal bars) are shown with their valence electron configuration nl to the left, the total angular momentum J on top (as a fraction), grouped by their term configuration 2^S+1L^P at the bottom row. Bound-bound permitted (solid lines) and forbidden (dashed lines) transitions connect the levels. PRD transitions are indicated in orange. Bound-free transitions (dotted lines) connect their levels to the Ca II continuum (hashed area). For all transitions, the line center or threshold wavelengths are given in Ångströms.

radiation, or in the 1.5D approximation by treating each vertical column as an independent plane-parallel atmosphere.

By default, the code treats line scattering with complete redistribution (CRD). We use a recent upgrade of the code (Sukhorukov & Leenaarts 2017) that allows us to treat resonance line scattering with partial redistribution (PRD) and cross-redistribution (XRD). For more details we refer to Sect. 3.4.

3.2. Model atom

We used a five-level plus continuum model atom of the Ca II ion illustrated in Fig. 2. It contains the lowest levels of Ca II that are sufficient to represent the physics of formation for the H, K, and infrared triplet lines together. The properties of the atomic levels are from the NIST Atomic Spectra Database following Sugar & Corliss (1985) for Ca II and Edlén & Risberg (1956) for Ca III.

Transition probabilities for the permitted transitions (H, K, and T) are from Theodosiou (1989). To ensure the correct population of the $3d\ ^2D^e$ term, we added the $3d\ ^2D^e-4s\ ^2S^e$ multiplet with two forbidden lines at 7291.4714 and 7323.8901 Å with transition probabilities from Osterbrock (1951). Both forbidden lines are present, although blended, in the solar spectrum (Grevesse & Swings 1968; Lambert et al. 1969; Lambert & Mallia 1969; Schorn et al. 1975; Day 1974). The broadening parameters of all lines are from the Vienna Atomic Line Database (Piskunov et al. 1995; Kupka et al. 1999) among which the van der Waals parameters are taken from Barklem et al. (2000).

Photoionization cross-sections for the bound-free transitions are from the TOPBase server of the Opacity Project (Seaton et al. 1994). The original cross-sections are sampled on a very fine 10^3-10^4 -point grid of frequencies with well-resolved resonance and autoionization transitions. For each atomic level in the model, we smoothed and downsampled the original data to ~ 30 -point grid following Bautista et al. (1998) and Allende Prieto et al. (2003).

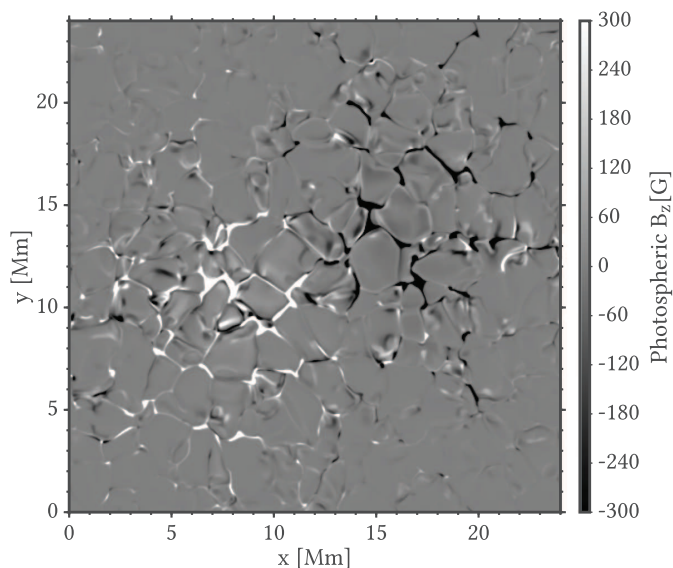


Fig. 3. Vertical magnetic field strength in the photosphere in Model 2, at the height where the average optical depth at 5000 Å is unity.

Bound-bound electron collisional rates are composed of data from Meléndez et al. (2007) and extrapolations following Burgess & Tully (1992). Bound-free collisional rates are either from Arnaud & Rothenflug (1985) for the ground $4s\ 2S^e$ level or from the general formula provided by Burgess & Chidichimo (1983) for the excited levels. We also include collisional autoionization (Arnaud & Rothenflug 1985) and dielectronic recombination (Shull & van Steenberg 1982).

We adopt a standard atomic weight of the Ca atom, 40.078 amu for a mixture of 96.9% ^{40}Ca , 2.1% ^{44}Ca , and 1.0% $^{42,43,46,48}\text{Ca}$ isotopes. The solar abundance of Ca is taken to be 6.34 on the standard $[H] = 12.00$ scale (Asplund et al. 2009).

3.3. Model atmospheres

As model atmospheres we used three snapshots from three different radiation-magnetohydrodynamic (R-MHD) numerical simulations carried out with the Bifrost code (Gudiksen et al. 2011). All three runs simulated a bipolar magnetic region, which consists of two magnetic polarity patches separated by 8 Mm (illustrated for Model 2 in Fig. 3). The region is similar to an enhanced network with an unsigned magnetic field strength of 50 G in the photosphere. In all three cases, the simulation box has the same physical size of 24 Mm \times 24 Mm \times 16.9 Mm spanning from the top of the convection zone up to the corona. The models differ in the spatial resolutions of their coordinate grids and in the equations of state (EoS) used for the initial R-MHD setup. We refer to these models as Model 1, Model 2, and Model 3. We selected and prepared all three models so that, compared to the diffraction-limited spatial resolution of SST/CHROMIS, their horizontal grid spacing is larger for Model 1, and is smaller for Model 2 and Model 3.

Model 1 is based on the public Bifrost model atmosphere published by Carlsson et al. (2016). We took a snapshot at $t = 3850$ s of solar time. The simulation used an EoS that includes the effects of non-equilibrium ionization of hydrogen (Leenaarts et al. 2007). The original model has $504 \times 504 \times 496$ grid points within the full physical extent of the simulations. We reduced the grid size of this model to save computational time. We clipped the vertical range of heights to $-0.48 \dots +14.2$ Mm keeping only

formation heights of the Ca II spectrum. We also halved the horizontal grid resolution by removing every other point in the XY-direction. The final model has $252 \times 252 \times 440$ grid points with a uniform horizontal grid spacing of 95 km and a vertical grid spacing ranging from 19 km in the photosphere and chromosphere to 96 km in the corona.

Model 2 was made using the same initial setup as Model 1. There are two differences. First, this simulation was carried out using a different EoS that includes effects of the non-equilibrium ionization of hydrogen and helium (Golding et al. 2014, 2016). Second, we took this snapshot at a different moment of simulation time, 780 s after the running code was switched from the LTE EoS to the non-equilibrium EoS of hydrogen and helium. We clipped the vertical range of heights to $-0.53 \dots +6.6$ Mm, but kept the original horizontal grid resolution. The final model has $504 \times 504 \times 336$ grid points with a uniform horizontal grid spacing of 48 km.

Model 3 has a different EoS setup. The ionization and recombination of hydrogen and helium were treated in instantaneous LTE, which means that the atomic number densities follow the Saha-Boltzmann equations. The original size of this model grid is $768 \times 768 \times 768$ points. We clipped the vertical range of heights to the same range as in Model 2 and we kept the original horizontal resolution. The final model has $768 \times 768 \times 476$ grid points with the uniform horizontal grid spacing of 31 km and a vertical grid spacing from 13 km in the photosphere and the chromosphere to 27 km in the corona.

A comparison of the different EoS effect on the temperature stratification, is provided in Golding et al. (2016).

3.4. Line treatment in CRD, PRD, and XRD

Contrary to many photospheric lines, which can be modeled assuming photon scattering with complete redistribution (CRD), the resonance doublet and the infrared triplet of Ca II are formed in the chromosphere and require a more accurate treatment of resonance photon scattering with partial redistribution. In PRD, the frequency and direction of the ingoing and outgoing photon in a scattering event can be correlated. To the contrary, they are independent in CRD.

In addition, as all the lines share the same upper term $4p\ 2P^o$ and have either sharp ($4s\ 2S^e$ for H and K) or metastable ($3d\ 2D^e$ for infrared triplet) lower terms, they all are affected by resonance Raman scattering of photons, often called “cross-redistribution” (XRD). Thus, a photon absorbed in one of the H, K, or infrared triplet lines can be emitted in the same line (resonance scattering) or in one of the other lines (resonance Raman scattering). A classical example of cross-redistribution in astrophysics is the formation of the H I Ly- β line (Hubeny & Lites 1995), which is interlocked with the H- α line.

Following Uitenbroek (1989), we tested the formation of all the five lines either in CRD or PRD, with or without XRD using various 1D models of the solar atmosphere. We found that PRD is essential for the H and K lines, but less important for the 8542 and 8662 Å lines. Cross-redistribution has very weak effect on the intensity profiles of the infrared triplet lines, but generally makes 2–10% intensity difference in the inner wings of the H and K lines. The 8498 Å line has the smallest transition probability and is formed mostly in the photosphere. It shows very little effects of PRD and makes no contribution with XRD to its subordinates, the K and the 8542 Å lines. We treated the 8498 Å line in CRD reducing the total computational time by 10%. Including XRD increases the total computational time by 35% compared to

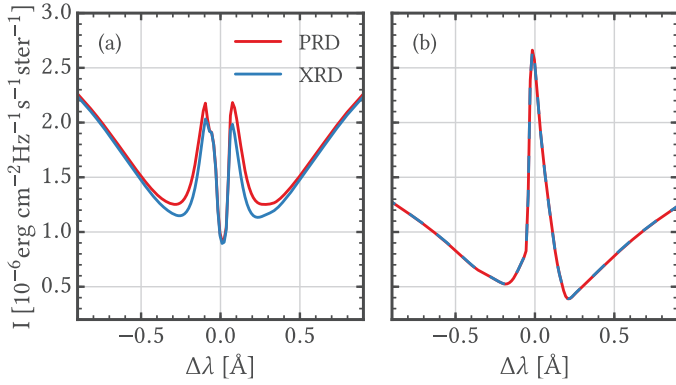


Fig. 4. Example profiles showing an effect (*left*) and no effect (*right*) of cross-redistribution (XRD; blue line) on the Ca II K intensity computed in 3D, extracted from two columns from Model 2 at $\mu = 1$. The same profiles computed with only partial redistribution but not cross-redistribution (PRD; red line) are given for comparison.

PRD. We treated the H, K, 8542 Å, and 8662 Å lines with XRD (orange in Fig. 2). Thus, photons can be either scattered resonantly in each of these lines, being absorbed and emitted in the same transition, or cross-redistributed in the 3968 Å \leftrightarrow 8662 Å as well as 3934 Å \leftrightarrow 8542 Å cascades, being absorbed in one and emitted in the other transition.

Cross-redistribution provides an extra escape route for photons absorbed in the H and K lines at heights where the subordinate infrared triplet lines are formed. Thus, mostly the inner wings and the outer slopes of the peaks of the H and K lines are affected, but not the cores as at those heights the infrared triplet lines are optically thin and scattering redistribution is dominated by thermal motions in the line cores. Figure 4 illustrates this effect in the synthetic profiles of the K line. Normally, XRD slightly decreases the intensity in the inner wings without much center-to-limb variation (see Fig. 5).

3.5. Effects of 1.5D/3D RT and CRD/PRD/XRD

Because they could not perform non-LTE 3D PRD computations, Leenaarts et al. (2013a) modeled the Mg II H and K lines with different treatments in the core and wing parts of the profile.

In the cores of resonance lines, the redistribution is close to CRD as it is controlled by random frequency shifts owing to thermal (Doppler) motions, which destroys the frequency-coherency of the scattering. As resonance lines are strong and highly scattering, their cores are formed higher up in the chromosphere where the effects of horizontal radiative transfer become essential, and 3D radiative transfer must be applied. Therefore, a 3D CRD treatment is reasonably accurate for the cores of such lines.

In the wings of resonance lines, PRD effects are more important because of the radiative damping is much larger than the collisional damping. Because the line wings are formed relatively deep in the atmosphere and the effect of horizontal radiative transfer is small there, a 1.5D PRD treatment can be used to approximate the wing intensity for such lines.

Sukhorukov & Leenaarts (2017) presented a method to perform radiative transfer computations in 3D non-LTE including PRD. Therefore we test the influence on the Ca II H and K lines of the simplifying assumptions of 1.5D XRD, 3D CRD, and 3D PRD compared to the most accurate treatment of 3D XRD.

Uitenbroek (1989) tested whether the inclusion of cross-redistribution influences the intensity and center-to-limb variation of the Ca II H line in a 1D model of the solar atmosphere. Here we perform a similar comparison, but now for a 3D atmosphere and including 3D radiative transfer. Figure 5 shows the center-to-limb variation of spatially averaged intensity profiles of the K line treated accurately in 3D XRD and approximately in 1.5D XRD, 3D CRD, and 3D PRD. We note that 3D effects are dominant in the line core although some coherency is still present as there is a small intensity difference compared to 3D XRD. Outside of the line core, the redistribution effects become dominant and 3D CRD produces large errors in the wings. The 3D CRD reach the redistribution intensities at $\Delta\lambda \approx \pm 3$ Å. The redistribution effects increase towards the limb as the difference between the 3D CRD and 3D XRD is increasing. The 1.5D RT approximation is accurate in the outer wings (at more than ~ 0.3 Å from line center) of the line but is not at the K₁ minima and K₂ peaks (see Sect. 3.6 for a definition of K₁ and K₂). On average, the cross-redistribution decreases the intensity in the inner line wings by 5–10%.

Figure 6 shows how the 3D XRD intensities are related to the approximate 1.5D XRD intensities at the emission peaks (K₂, see Sect. 3.6) and the approximate 3D CRD intensities at the central line depression (K₃) for all profiles in Model 1. At the core, the accurate and approximate intensities are linearly related and the 3D CRD approximation overestimates radiation temperatures by less than 50 K. At the emission peaks, there is a saturation effect in 1.5D XRD depending on the range of observed intensities. Below 4.5 kK intensities are underestimated by 300 K, above 5 kK intensities are overestimated by 200 K, in between intensities are accurate. This is similar to what was observed for the Mg II h and k lines (Sukhorukov & Leenaarts 2017), although these lines are not affected by cross-redistribution.

Therefore, the K line intensity can only be accurately modeled if the effects of 3D radiative transfer and XRD are considered together. The same is true for the H line.

Throughout the rest of this paper, we derive our results from the synthetic Ca II H and K data that were computed with the combined effects of non-LTE, 3D radiative transfer with XRD.

3.6. Line profile features

The diagnostic properties of the Ca II H and K lines can be investigated with techniques of various complexity. The easiest technique is to search how a single line parameter, for example an equivalent width or a central depth, is related to some general property of the model atmosphere, which is computationally and practically easy but is only of limited use. The most elaborate technique would be solving the inverse problem of radiative transfer in the H and K lines to restore the whole structure of the atmosphere at formation heights of the lines. This is in principle possible in the 1.5D approach (de la Cruz Rodríguez et al. 2016), where each pixel is treated as an independent atmosphere, but not with full 3D radiative transfer.

We chose a procedure of intermediate complexity similar to what was carried out by Leenaarts et al. (2013b), as the Mg II h and k and the Ca II H and K lines are formed in a similar way and have similar line profile shapes. First, we synthesized the H and K intensity profiles, next we classified the synthetic profile features, and finally we correlated the properties of the features with the parameters of the model atmosphere at their formation heights.

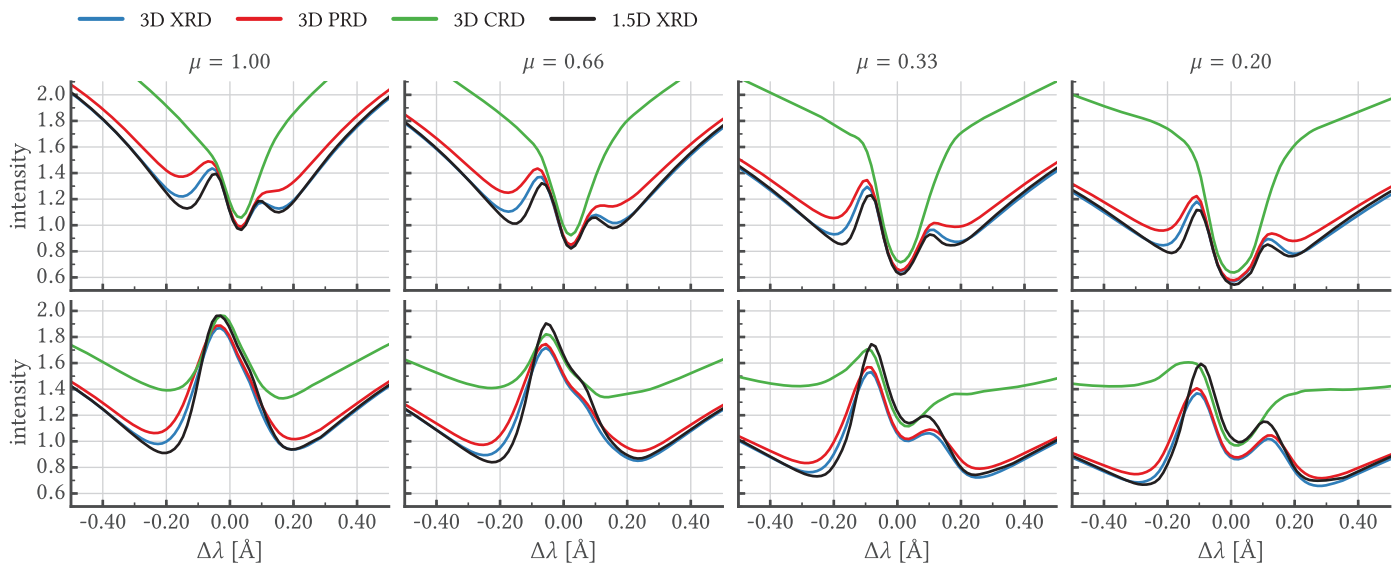


Fig. 5. Spatially averaged intensity profiles of the Ca II K line computed using Model 1 (*upper row*) or Model 2 (*lower row*) at four different angles: $\mu = 1.0, 0.66, 0.33,$ and 0.2 (*columns from left to right*). Results are given for 3D XRD (blue), 3D PRD (red), 3D CRD (green), and 1.5D XRD (black). The intensity units are $10^{-6} \text{ erg s}^{-1} \text{ cm}^{-2} \text{ Hz}^{-1} \text{ ster}^{-1}$.

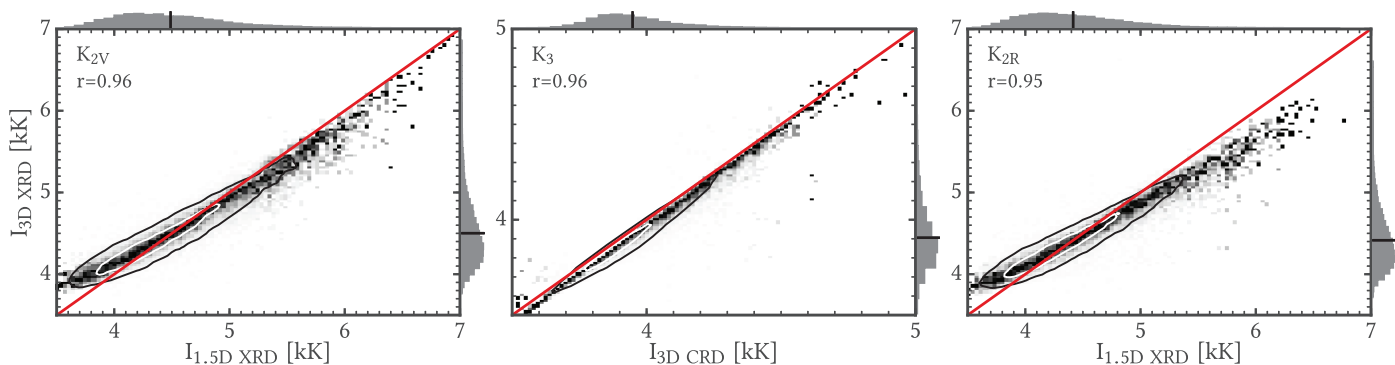


Fig. 6. Joint-PDF distributions of the brightness temperature in K_{2V} (*left*), K_3 (*center*), and K_{2R} (*right*) for different combinations of the radiative transfer geometry (1.5D or 3D) and the line scattering (CRD or XRD). Intensities are calculated using Model 1 atmosphere at $\mu = 1$. The red line is $y = x$. The correlation coefficient r is given on each panel. Contours encompass 50% (white) and 90% (black) of the pixels. Each column in the Joint PDF is scaled to maximum contrast. The short black lines at the univariate histograms (each panel’s top and right) show mean values.

We classified the profile features for the H and K lines using the notation system introduced by Hale & Ellerman (1904) for “standard” Ca II K line-core profiles with two emission peaks close to the line core. Arriving from the short-wavelength side the first minimum is denoted as K_{1V} , the first emission peak is K_{2V} , the central minimum is K_3 , the second peak K_{2R} and the third minimum is K_{1R} . The H line is characterized similarly.

We wrote a feature-finding code to classify the line profiles in each pixel of each of the three models. Standard profiles (see Fig. 7a) follow the classification described above.

If we find only one emission peak (as in Fig. 7b), we assign this peak either to the 2V or the 2R feature depending on which side the peak lies with respect to the nominal line center. We find that very often the 3-feature can be mistaken for a 1-feature if the true line core (i.e., the wavelength with the largest $\tau_v = 1$ height) is hidden in the slope of the single 2-feature owing to a strong velocity gradient. We therefore assigned the 3-feature to the lowest intensity minimum next to the emission peak. The other remaining minimum is the 1-feature. If the total shift of both the minima off the line center is more than 75 km s^{-1} , then there is no 3-feature and the minima are the 1V- and 1R-features.

In 1–2% of the single-peaked profiles, the wavelength of the peak actually has the largest $\tau_v = 1$ height. This happens when the source function is monotonically increasing with height in the chromosphere. This is rare in our quiet-Sun-like atmosphere models, but might be more common in simulations with stronger magnetic activity.

If the profile has only one minimum and no peaks as in Fig. 7c then we only assigned the 3-feature.

The most common complication is when the profile has more than two emission peaks as in Fig. 7d. We then assigned the features based on rules that were empirically determined to give a reasonable result.

We note that the feature-finding algorithm still produces many incorrect identifications. Averaged over all three model atmospheres, we got the following fractions of the Ca II profile types: 1% pure absorption, 16.5% one emission peak, 61% two emission peaks, and 21.5% several emission peaks. Model 2 has the strongest velocity gradients in the chromosphere and produces 80% more many-peaked profiles than Model 1 or Model 3. As the classifying algorithm is ambiguous for many-peaked profiles, we have the largest uncertainties with Model 2.

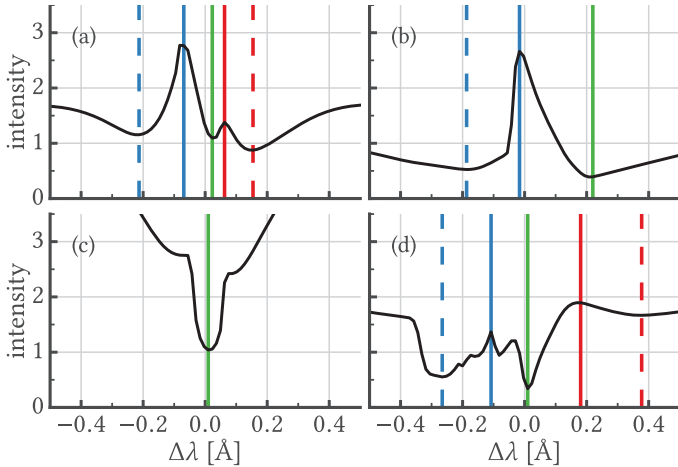


Fig. 7. Feature classification examples for the Ca II K line computed using Model 2. The intensity profile (solid black) is crossed by vertical lines denoting the K_{1V} (dashed blue), K_{2V} (solid blue), K_3 (solid green), K_{2R} (solid red), K_{1R} (dashed red) features. *Panel a:* standard profile with two emission peaks is shown. *Panel b:* single-peaked emission is represented. *Panel c:* pure absorption is shown. *Panel d:* complex profile with multiple emission and absorption features is represented. Intensity units are $10^{-6} \text{ erg cm}^{-2} \text{ Hz}^{-1} \text{ s}^{-1} \text{ ster}^{-1}$.

3.7. Synthetic data degradation

To compare our observations with our computations, we degraded the synthetic Ca II K data to match the spatial and spectral resolution as well as the wavelength sampling of SST/CHROMIS.

First, we convolved each synthetic image with the spatial PSF of the instrument, a 2D Gaussian kernel having $FWHM = 0''.1$. Second, we convolved each synthetic spectral profile with the measured transmission profile of the CHROMIS filter having $FWHM = 120 \text{ mÅ}$ at 3930 Å . Third, we binned synthetic images to match the spatial pixel size of the instrumental CCD chip, $0''.0375$. The physical extent of the synthetic image, $24 \text{ Mm} \times 24 \text{ Mm}$, maps to 884×884 pixels on the CCD chip. Fourth, we sampled synthetic spectral profiles at wavelengths corresponding to the wavelength grid without the continuum point along one scan of the CHROMIS observations (see Sect. 2). For each of the three atmosphere models, the resulting data is an array of $884 \times 884 \times 35$ values along the (X, Y, λ) -directions.

We do not include any degradation of the synthetic data to for instrumental straylight or residual effects of atmospheric turbulence. We therefore expect the synthetic images to have a considerably higher contrast than the observations.

4. Formation of Ca II H and K

In this section we discuss how the Ca II H and K are formed and display four exemplary line profiles from our 3D XRD computations. We only discuss the K line, since the H line forms in the same way.

4.1. An illustration of the formation of Ca II H and K

The formation of the Ca II H and K lines are severely complicated by velocity fields, PRD/XRD effects, and the highly in-homogeneous temperature structure of the solar chromosphere (examples are shown in Sect. 4.2). To set the stage, we

used the 1D FAL-C model atmosphere (Fontenla et al. 1993) to illustrate the basic formation of the Ca II K line in a four-panel Eddington–Barbier diagram. The PRD adds an extra complexity to the analysis, by making the line source function frequency-dependent. To keep things somewhat simpler, we use the CRD approximation here, which means that the line source function is independent of frequency.

Figure 8 shows 2×2 formation diagrams following Rutten (2003) for three different computations: the FAL-C temperature structure without microturbulence, with a constant microturbulence (5 km s^{-1}), and a computation with constant microturbulence (5 km s^{-1}), but with a modified temperature structure. The microturbulence, ξ , is an ad hoc parameter used to broaden the spectral lines to fit the observed spectral lines. We note that the model atmospheres from Bifrost do not include microturbulence.

Panel c in Fig. 8 shows the vertical emergent intensity for the Ca II K line. Panel b shows the optical depth as function of height at the wavelengths of the K_{2V} and K_3 features. The emission peak, K_{2V} , is formed at the maximum of the line source function, which is shown in panel d. The line source function is only partially coupled to the chromospheric temperature rise. The K_3 feature is formed at the largest formation height at 1.9 Mm for all the cases. Panel a shows the broadening effect on the extinction profile from the microturbulence. Panel c shows that the microturbulence (5 km s^{-1} in this case) increases the K_2 separation by a factor 3 compared to the case without microturbulence.

Panel d shows two different temperature stratifications, illustrating how the depth at which the chromospheric temperature rise is located affects the emergent line profile. The K_2 separation increases slightly and the K_1 location shifts outward to $\Delta\lambda = \pm 1.5 \text{ Å}$ with the deeper temperature rise shown in panel c.

4.2. Analysis of line intensity formation

We discuss the formation of four example K line profiles using the method of Carlsson & Stein (1997) computed in 3D XRD with Model 2. We decomposed the contribution function to the emergent intensity

$$C_I(\nu, z) \equiv \frac{dI(\nu, z)}{dz} = \frac{\chi(\nu, z)}{\tau(\nu, z)} \cdot S(\nu, z) \cdot \tau(\nu, z) \exp(-\tau(\nu, z)) \quad (1)$$

into three components, χ/τ , S , and $\tau \exp(-\tau)$, which we plot side by side in a 2×2 panel diagram showing the dependence on the frequency ν along the X -axis and the dependence on the height z along the Y -axis. On each panel we overplot optical depth unity as a function of frequency $z(\tau_\nu = 1)$, and the vertical velocity $v_z(z)$.

The first component is the ratio of the total (line plus continuum) opacity χ to the optical depth τ . It is dominant at small optical depths and is sensitive to the line-of-sight velocity gradient.

The second component is the total source function S , which is frequency-dependent for PRD lines. To emphasize this feature, we plot the source function S in temperature units along the redward and blueward slopes of the $z(\tau_\nu = 1)$ curve. We also show the local gas temperature.

The third component $\tau \exp(-\tau)$ outlines where the optical depth τ equals unity.

The contribution function C_I is shown on the last panel together with the emergent intensity profile $I(\nu)$.

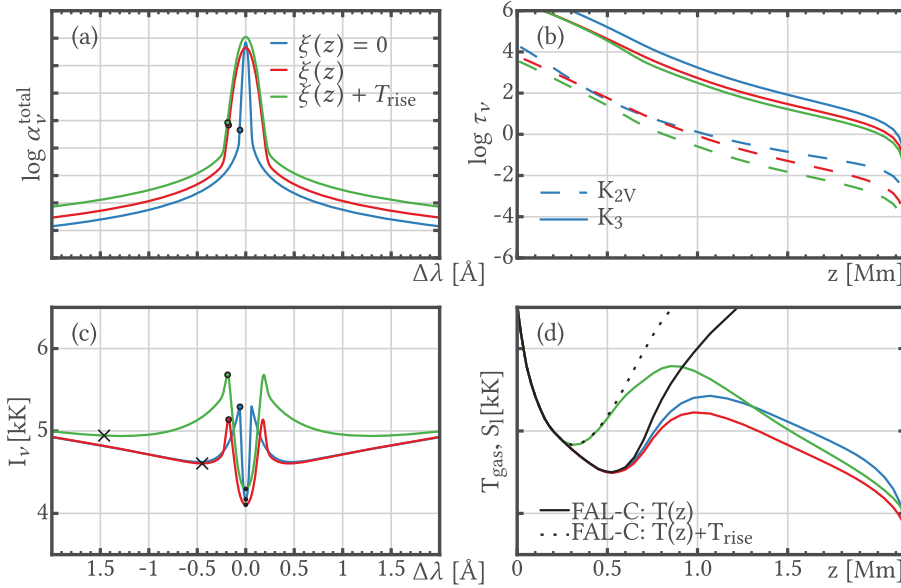


Fig. 8. A four-panel Eddington–Barbier line formation diagram for the Ca II K from the FAL-C model atmosphere in CRD. The computations are performed with three different cases: without microturbulence ($\xi(z) = 0$ km s⁻¹; blue line), microturbulence ($\xi(z) = 5$ km s⁻¹; red line), and with a deeper temperature rise and microturbulence (green line). *Panel a:* the total opacity as function of wavelength at the formation height of the peaks; *panel b:* the optical depth as function of height at the wavelength of at K_{2V} (dashed) and K₃ (solid); *panel c:* the vertically emergent intensity for the K line, and *panel d:* the gas temperature as a function of height (solid and dashed black) with the line source function (solid colored). The cross marks the position of K_{1V} in *panel c* and the dot indicates the position of the K_{2V} in *panel a* and K_{2V}/K₃ in *panel c*.

Figure 9 provides 2×2 diagrams for four types of intensity profiles that we used to classify the features. A normal profile with two emission peaks (subfigure a), a profile with a single emission peak (subfigure b), a pure absorption profile (subfigure c), and a profile with a large peak-to-peak separation (subfigure d).

Subfigure a shows the formation of a normal profile with two emission peaks and K_{2V} is stronger than K_{2R}. The positive asymmetry is caused by a combination of an upflow at 1.2 Mm and a downflow at 2.4 Mm and by an enhancement of the source function at 1.2 Mm. K_{2V} is formed at 1.3 Mm with $T_b = 4.9$ kK, which is roughly 500 K lower than the gas temperature at the same height. K_{2R} is formed at 0.9 Mm and has an upper-chromospheric contribution from 2.1 Mm. K₃ is well-formed as a central depression formed at the maximum formation height of 2.2 Mm and its Doppler-shift matches the vertical velocity at this height.

The PRD effects add an extra complexity to the analysis. The line source function is not constant anymore and varies strongly with wavelength. The source function starts decoupling from the Planck function already at ± 30 km s⁻¹ around the line core and then it strongly diverges at ± 12 km s⁻¹.

Subfigure b shows a profile with a single emission peak. This shape is caused by a strong downflow at 1.5–1.9 Mm in the wake of a shock wave that has passed before. This profile has no K₃, and the maximum formation height is located in the blue slope of the emission peak at $\Delta v = -10$ km s⁻¹. The only emission peak is formed at 1.6 Mm and is identified as K_{2V}, which is on the blue side off the line center, at $\Delta v = +2$ km s⁻¹. The source function and Planck function are decoupled from each other at K_{2V}. The difference in the observed brightness and local gas temperatures is 2.1 kK. The source function and Planck function are almost coupled at K_{1R} and K_{1V} located at $\Delta v = -13$ km s⁻¹ and $\Delta v = +12$ km s⁻¹, respectively, so that the brightness temperature at both minima corresponds to the local temperature.

Subfigure c shows a pure absorption profile. Throughout the entire range of the formation heights, the vertical velocity does not exceed 2.5 km s⁻¹. This makes the formation height profile almost symmetric around the line center and the shape of the intensity profile is mostly defined by the variation of the source function with height. The source function is well coupled to the Planck function up to 0.6 Mm and they follow a very flat slope.

These absorption profiles usually appear if the vertical velocity amplitude is small and the chromosphere is cold without a strong temperature increase.

Subfigure d shows a profile with large peak-to-peak separation. Both emission peaks, at ± 27 km s⁻¹, are caused by a deep chromospheric temperature rise at $z = 0.35$ Mm. The emission peaks are symmetric because the vertical velocity is only 1 km s⁻¹ at the formation height. The source function decouples from the Planck function at 0.4 Mm and decreases toward the maximum formation height at 2.7 Mm, forming the central core.

5. Comparison between observations and simulations

We compared our synthetic data with the SST/CHROMIS observations made in the K line. We also tried to reproduce some general properties of the K line in the solar spectrum using older data. As the H and K lines share many common properties and are formed in the chromosphere in practically the same way, we expect our conclusions to be similar for both of these lines.

The primary reason to prefer the K line to the H line is that the former has a factor two higher opacity and therefore is formed slightly higher in the chromosphere. This allows us to probe the largest height range in the atmosphere. In addition, the H line typically has less pronounced H_{2V} and H_{2R} emission peaks.

Another practical reason is that the H line is blended with the H- ϵ line of H I at 3970.075 Å, that is, in the red wing just next to the H_{1R} feature.

5.1. Spatially averaged Ca II K spectrum

We compared spatially averaged intensity profiles of the K line from our simulations computed with 3D XRD with spatially averaged profiles from our observations and high-resolution profiles from the Hamburg quiet-Sun disk-center intensity atlas (Neckel & Labs 1984; Neckel 1999).

Figure 10 (top) relates undegraded profiles from our calculations to the atlas profile measured with $\lambda/\delta\lambda = 4.5 \times 10^5$ resolution. The atlas profile shows distinct K_{1V}, K_{2V}, K₃,

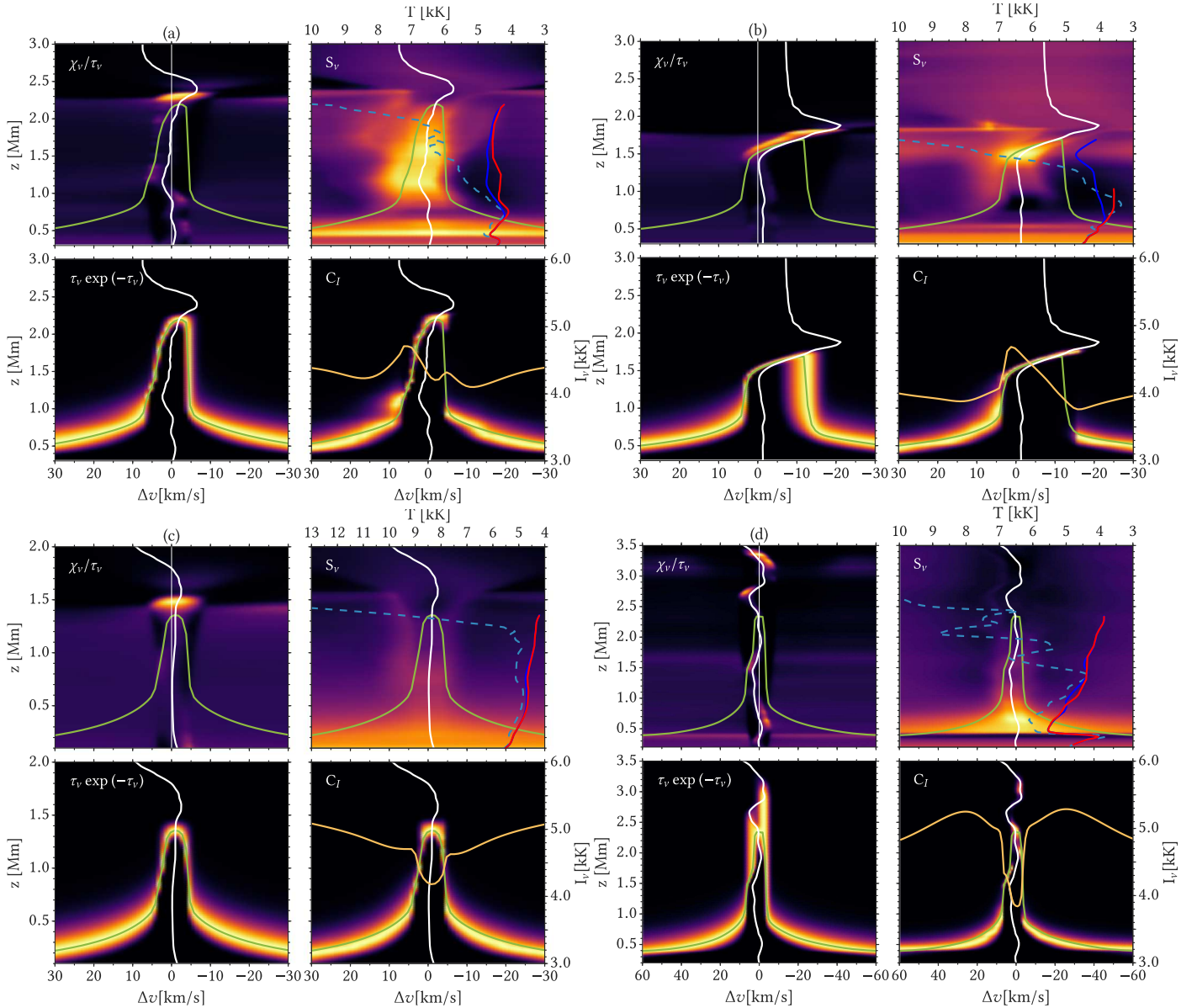


Fig. 9. Intensity formation breakdown figure for the Ca II K line from Model 2. *Subfigure a:* normal profile with two emission peaks is depicted. *Subfigure b:* profile with a single emission peak is shown. *Subfigure c:* pure absorption profile is shown. *Subfigure d:* profile with a large peak-to-peak separation is depicted. Each image (black corresponds to low values, yellow to high values) shows the quantity specified in its top left corner as a function of frequency from line center (in Doppler shift units) and simulation height z . Multiplication of the first three produces the intensity contribution function in the *fourth panel*. A $\tau_v = 1$ curve (green) and the vertical velocity (white solid, positive is upflow) are overplotted in each panel; a $v_z = 0$ line is indicated in the *first panel* for reference. The *upper right panel* also contains the gas temperature (dashed) and the line source function along the $\tau = 1$ curve in blue for the part of the τ curve blueward of its maximum value and red for the part on the red side of the maximum $\tau = 1$ height, in temperature units specified along the top. The *lower right panel* also contains the emergent intensity profile (orange), as brightness temperature with the scale along the right-hand side.

K_{2R} , and K_{1R} features, in which K_{2V} is stronger than K_{2R} and separated by 0.3 \AA , and K_3 is shifted by -0.03 \AA off the nominal line center. The two separated emission peaks are reproduced by Model 1 and Model 3, while they are blended together in Model 2 and separate only toward the limb (see Fig. 5 and Sect. 5.2). The peak separation in all three models is less than one half of the peak separation in the atlas profile. The same is true for the K_{1V} -to- K_{1R} distance, which is the biggest, but still insufficient, in Model 2. The peak asymmetry is correct in Model 3, stronger in Model 2, and too big in Model 1. Peak intensities are too low in Model 1 and Model 3 and too high in Model 2. The opposite is true for the line core intensities. The

K_3 core is redshifted in Model 1 and Model 3 and might be at the right position in Model 2 as the blended peaks are slightly blueshifted off the line center. The K_1 features and the inner wings have a lower intensity in the simulations than in the atlas, except for the outer wings in Model 1, which are brighter than in the atlas profile.

Figure 10 (bottom) relates the spatially averaged profile observed with SST/CHROMIS with the simulated line profiles degraded to CHROMIS spectral resolution.

In the observed profile, we can still recognize all the features although K_{2R} is only a small bump in the red flank of the line and not a clear local maximum. The peak asymmetry and K_2

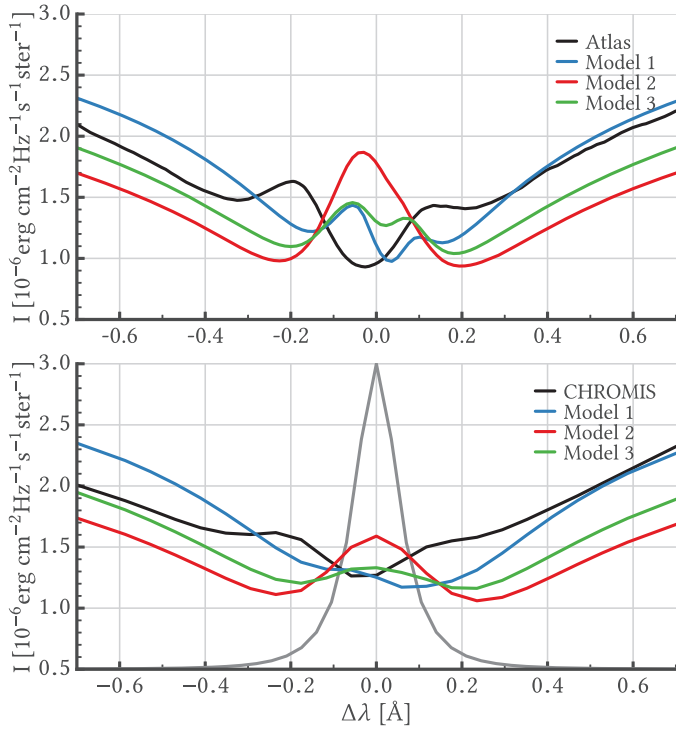


Fig. 10. Spatially averaged intensity profiles of the Ca II K line at $\mu = 1$. *Upper panel:* undegraded synthetic profiles for Model 1, 2, and 3 (blue, red, and green) are compared with the Hamburg atlas profile (black). *Lower panel:* degraded synthetic profiles (same notation) are compared with the SST/CHROMIS profile from our observations (black). The gray curve indicates the assumed CHROMIS spectral transmission profile.

intensities are reduced, while the K_3 intensity is increased. The wavelength positions and the corresponding separations of the features are almost unaffected. The spatial and spectral resolution of the instrument smooth out small spectral features in the synthetic data so that the K_3 core disappears and the K_2 features cannot be resolved as two separate peaks. The K_1 and inner wing intensities remain roughly the same while the K_2 intensities are reduced.

None of the models reproduce both the full-resolution and the degraded K line profiles. The models appear either too cold or too hot in the upper photosphere, and they are too cold around the temperature minimum and are either too cold or too hot in the middle chromosphere, where non-thermal broadening is not strong enough in the simulations.

5.2. Center-to-limb variation

Center-to-limb observations of the solar Ca II K spectrum show two effects (see, e.g., Engvold 1966; Zirker 1968). First, all their intensities undergo limb darkening. Second, the K_1 and K_2 separations increase toward the limb. First shown by Shine et al. (1975) and later confirmed by more accurate modeling by Uitenbroek (1989), the H and K lines must be treated in PRD as modeling assuming CRD cannot reproduce any of the center-to-limb effects. However, it is not possible to accurately model both effects using the same 1D model atmosphere (Shine et al. 1975).

We tested whether we can reproduce both center-to-limb effects in Model 1 and Model 2. We computed spatially averaged K-line intensities at $\mu = 1.0, 0.66, 0.33,$ and 0.2 in the

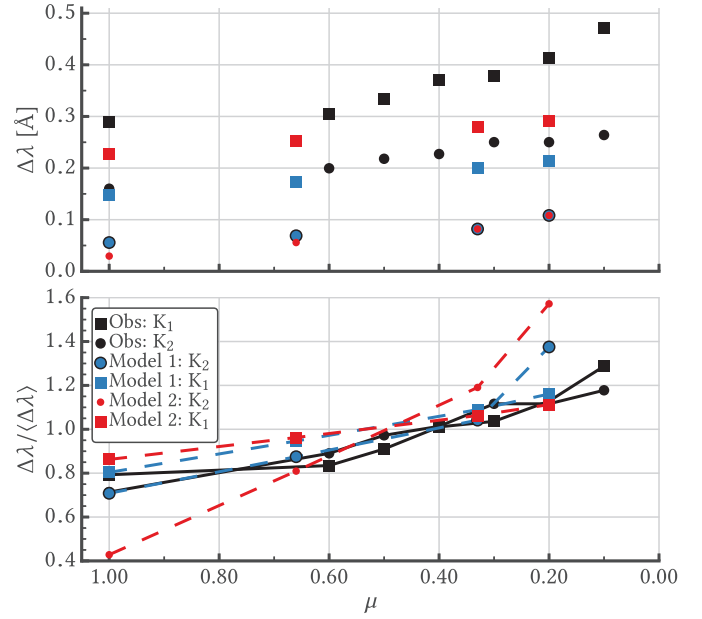


Fig. 11. Center-to-limb variation of K_{1V} and K_{2V} distances off the line center observed by Zirker (1968) and Shine et al. (1975) (black markers), and computed for Model 1 (blue markers) and Model 2 (red markers) for the spatially averaged spectrum of Ca II K. *Upper panel:* absolute distances $\Delta\lambda$ to the features at different μ angles are shown. *Lower panel:* trends of $\Delta\lambda$ variations normalized to the mean $\langle\Delta\lambda\rangle$ in each group are shown.

most accurate 3D XRD treatment. We computed the intensity output for two azimuths, 0° and 90° , that is, along the X-axis and the Y-axis, and four different latitude directions having $\mu_Z = 1, 0.66, 0.33,$ and 0.2 . For each latitude we averaged over the two azimuths. For comparison, we adopted the observations taken with the Sacramento Peak Observatory spectrograph (Zirker 1968; Shine et al. 1975) from the disk center toward the south pole of the Sun, with the slit aligned in the North-South direction and an exposure time of 30 s.

Figure 5 illustrates the first center-to-limb effect in the K line. All features and the inner wings of the K line undergo a limb darkening in both model atmospheres, that is, their intensities steadily decrease toward the limb. We note that the emission peaks at K_{2V} and K_{2R} and the outer minima at K_{1V} and K_{1R} become more separated toward the limb.

Figure 11 relates the observed and synthesized distances of K_{1V} and K_{2V} off the line center. In this figure, we show variations of the absolute values (upper panel) and slopes of their trends (lower panel).

We note the same problem discussed above that the calculated K_1 separations are much smaller than the observed separations. Model 1 produces less than 50% and Model 2 produces 70–80% of the observed widths. The K_{1V} features show similar trends in both models. These trends are flatter than the observed trend. The K_{2V} features show very steep trends in both models, while the observed K_{2V} trend is a bit less steep than the observed K_{1V} trend.

Although neither model atmospheres reproduce correct separations between the corresponding features, they do reproduce the observed trends in center-to-limb behavior. In a certain sense, Model 1 fits better as it does not show the extreme trends of Model 2.

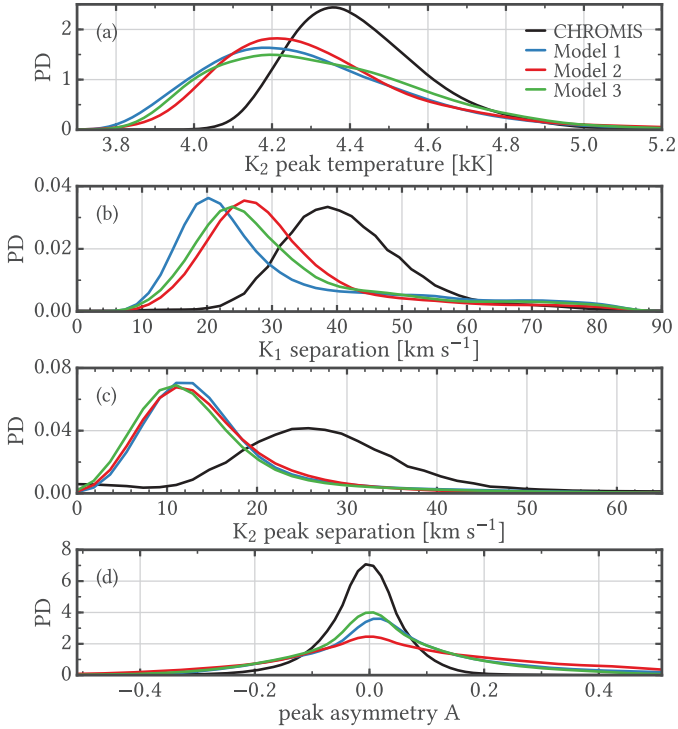


Fig. 12. From top to bottom: distributions of the K_{2V} and K_{2R} radiation temperature, K_1 separation, K_2 peak separation, and peak asymmetry in the SST/CHROMIS observations (black) compared to the simulations in Model 1, 2, and 3 (blue, red, and green) for $\mu = 1$.

5.3. Statistics of the Ca II K line parameters

Using the observed CHROMIS data set and our synthetic data sets, we investigated the distributions of four observable K-line parameters: (1) the brightness temperature at the K_2 emission peaks $T_b(K_2)$; (2) the wavelength separation between the K_1 minima; (3) the wavelength separation between the K_2 maxima; and (4) the peak asymmetry

$$A = \frac{I(K_{2V}) - I(K_{2R})}{I(K_{2V}) + I(K_{2R})}. \quad (2)$$

We spatially degraded the synthetic data set as in Sect. 3.7. The simulated emission peaks are roughly a factor 2.1 narrower than the observations, as shown in Fig. 10. Degrading with the spectral resolution of CHROMIS (120 mÅ) would lead unrealistically to many single-peaked profiles and K_2 intensities that are too low and K_1 intensities that are too high. We therefore smeared with a Gaussian of $120/2.1 \text{ mÅ} = 57 \text{ mÅ}$, where the factor 2.1 comes from the difference in emission peak width. This lower value is chosen so that the simulated profiles are smoothed, just as in the observations, but not so much that the emission peaks blend together. We note that this comparison is somewhat unfair. However, given the difference in the width of the central emission peaks, it allows a reasonable comparison of the distribution of the profile parameters.

Figure 12 shows distributions of all four parameters in the observations and simulations. The models predict K_2 brightness temperature that is too low compared to the observations, most likely caused by a temperature that is too low in the middle chromosphere in the simulations. The median brightness temperature in the simulations is 4.2 kK, while the observed brightness temperature is 4.4 kK. The straylight contamination

in the observations can affect the $T_b(K_2)$ distribution by decreasing its dynamical range of temperatures, so the real discrepancy between observations and simulations might be smaller than implied by the distributions.

The mean K_1 separation is smaller in the models than is observed, and their distribution has a long asymmetric tail toward high values, while the observed distribution is more symmetric. Likewise, the simulated K_2 separations are on average lower and show a tail in the distribution toward high values. The observed distribution is more symmetric. The K_1 and K_2 separation distributions are not sensitive to straylight contamination and the disagreement between the models and observations means that physical processes that produces non-thermal line broadening are missing or not sufficiently strong in the models. Previously, similar effects have been reported for Model 1 by Leenaarts et al. (2013b) for the Mg II h and k lines and by Rathore & Carlsson (2015) for the C II 1335 Å triplet.

Finally, the peak asymmetry shown in the bottom panel of Fig. 12 can be used to assess strong velocity gradients caused by shock waves traveling upward in the chromosphere (Carlsson & Stein 1992, 1997). It is known from observations (e.g., Grossmann-Doerth et al. 1974; Cram & Dame 1983; Rezaei et al. 2008) that K_{2V} is usually stronger than K_{2R} meaning that the peak asymmetry is slightly negative. All three distributions are centered around zero showing mean values of -0.01 (observations) and 0.01 – 0.04 (simulations). The observed distribution is negatively skewed with a bit longer tail of negative values and it goes from -0.3 to 0.2 . The synthetic distributions are positively skewed with a fairly long tail of positive values and they go from -0.3 to 0.5 . The synthetic distributions are wider. The closest, although not good, agreement with the observations appears in Model 3. The observed peak asymmetry distribution is not very sensitive to straylight. The model distributions might be influenced by the fact that we use a single snapshot from each simulation run. The mean and skewness of the distribution might depend on the phases of the global box oscillations that are present in the simulations (see Fig. 8 of Carlsson et al. 2016).

5.4. Images in the Ca II K line

We investigated whether Bifrost simulations reproduce similar chromospheric structures as we see in observed Ca II K images. Figure 13 relates line-wing and line-core images observed with SST/CHROMIS to similar images synthesized using the three Bifrost model atmospheres. Again, we spatially smeared the simulated images to SST/CHROMIS resolution, but smeared spectrally with a Gaussian with $FWHM$ of 57 mÅ. Smearing the simulated images with the full CHROMIS profile leads to too much mixing of low-chromospheric signal in the line-core images, and would not allow us to compare the fibril structure formed in the mid and upper chromosphere. We stress again that this is not a fair comparison of the imagery, and the small peak separation in the synthetic profiles is a clear indication that the chromosphere is not yet modeled correctly in the Bifrost models.

The line-wing images were observed and simulated close to the K_{1V} features, so they sample the upper photosphere just below the temperature minimum. We see regular brightness patterns in all four cases. These patterns come from reversed granulation, acoustic wave fronts and magnetic features. The Bifrost models show a brightness pattern with similar spatial scales in the most quiet regions (in the corners) as in the observations but with larger spatial scales between the two polarities in the central part of the field of view. This region has flux

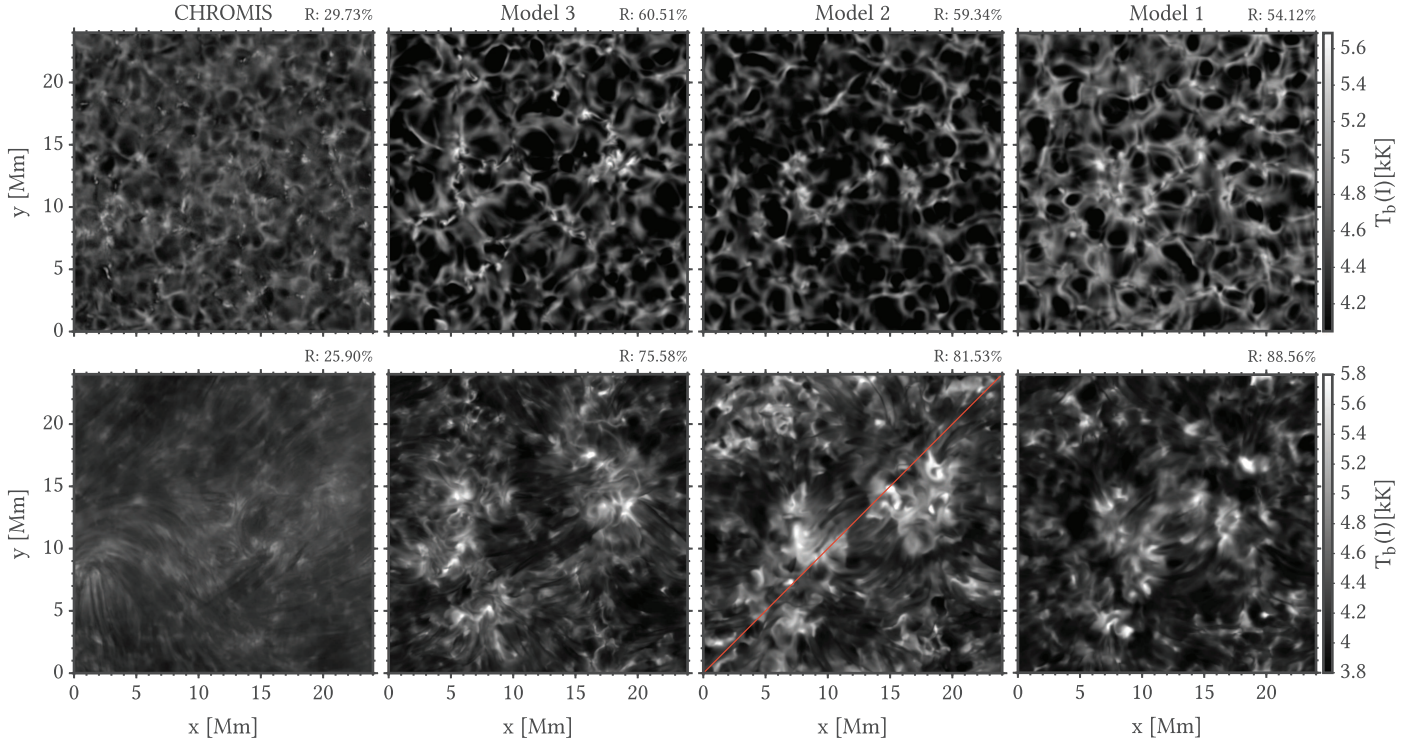


Fig. 13. Observed and simulated Ca II K images of the quiet Sun at the disk center ($\mu = 1$). *Upper row:* line wing at $\Delta\lambda = -0.528 \text{ \AA}$ is shown. *Lower row:* line center at $\Delta\lambda = 0 \text{ \AA}$ is shown. SST/CHROMIS images (*first column*) are compared with simulated images using Model 3, 2, and 1 (*second, third, and fourth columns*). Images are given in brightness temperature units with scales common for each row, specified at the right. The rms contrast R is provided in the upper right corner above each image. The red line indicates the slice through Model 2 shown in Fig. 15.

emergence in the simulations and also larger size granules. All the simulations show higher contrast compared to the observations. On average, Model 2 and Model 3 are darker and Model 1 is brighter than the observations. The typical size of magnetic field concentrations in intergranular lanes is also larger in the synthetic images: they appear as bright tiny dots of 4.8–5.1 kK in the observations while in the simulations they look like bright, diffuse, and elongated spots of 5.0–5.2 kK. Cold granular patches can be very dark in the simulations, with values below 4.0 kK, while in the observations they are somewhat higher, typically 4.1–4.2 kK.

The line core images in Fig. 13 show images at the nominal line center. The observations show a rather diffuse pattern of reversed granulation and subcanopy shock waves away from magnetic field concentrations; the superimposed fibrillar structure appears semi-transparent. The fibrils are thin (less than 0.3 Mm wide), typically 5–10 Mm long, and many originate at bright patches of magnetic concentrations seen in the observed line-wing image. The observed fibrils cover the whole field of view, and they are typically only slightly curved.

The synthetic images have a higher contrast than the observations. The areas above the photospheric magnetic elements are bright. The 96 km resolution Model 1 shows only a few fibrils, Model 2 with 48 km resolution shows more, and Model 3 with 31 km resolution shows most. The fine fibrils in Model 3 are very reminiscent of the observed fibrils. Still all models show too few fibrils and too strong visibility of the underlying shocks and reversed granulation. The numerical simulations have a horizontal grid spacing of 31 or 48 km. The smallest structures that can be formed in the simulation are roughly four times the grid spacing and are thus of comparable size or larger than the spatial resolution of CHROMIS/SST. Simulations with higher spatial

resolution are thus required to resolve the smallest observable scales.

The hottest network structures are brighter than 5 kK in the simulations and have only 4.7–4.9 kK in the observations. The coldest internetwork patches are colder than 4.1 kK in the simulations and are 4.1–4.2 kK in the observations.

We conclude that visually Model 3 shows more fine details than Model 1 or Model 2, and the structures in Model 3 are more similar to the observed chromospheric structures than those in Models 1 and 2.

In terms of the root-mean-square contrast of the intensity, all Bifrost models produce a factor of 1.8–2.0 higher contrast in the line wing and a factor of 2.9–3.4 higher contrast in the line core in comparison with the observations. This discrepancy is at least partially caused by the straylight contamination, which we did not correct for in the reduction procedure.

6. Diagnostic potential of the H and K lines

We used undegraded synthetic K-line spectrograms to demonstrate which properties of the line profile are useful for diagnosing the chromosphere. We only discuss the results for the K line, because the H line is formed in the same way. In some sections we employed only one model atmosphere out of three because the other models show similar results.

6.1. Formation heights of the profile features

We identified the K-line profile features in all three model atmospheres and measured corresponding formation heights. The zero point for the formation height is defined as the average height where the optical depth at 5000 Å is unity. Using the

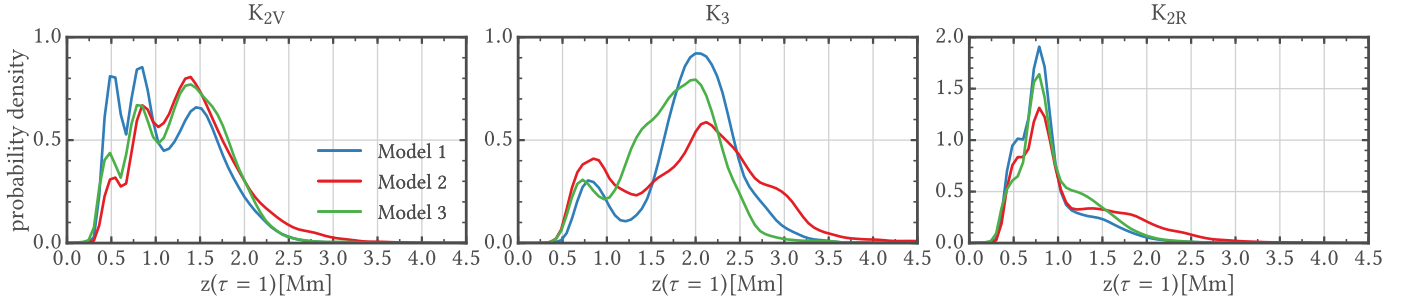


Fig. 14. Formation heights of K_{2V} (left), K_3 (middle), and K_{2R} (right). The zero point is defined as the average height where the optical depth at 5000 \AA is unity. Distributions show the probability density for heights where the optical depth equals unity in Model 1 (blue), Model 2 (red), and Model 3 (green).

Eddington–Barbier approximation at $\mu = 1$, we define the formation height z at a given frequency ν as the height where the optical depth equals unity, $\tau_\nu = 1$. Figure 14 shows the obtained distributions of $z(\tau_\nu = 1)$ at the frequency of the K_2 and K_3 features.

The K_3 feature is formed in the widest range of heights at $0.5\text{--}4.0 \text{ Mm}$. The side lobe on the left side of the distribution near $0.5\text{--}1.0 \text{ Mm}$ consists of pixels for which the feature-finding algorithm failed. Less than half of these are when K_3 is mistaken for K_1 around a single emission peak (see Sect. 3.6). The rest are when K_3 is mistaken for some local minimum in a complex profile with many emission peaks. Such local minima are formed between the upper photosphere and lower chromosphere. On average, K_3 forms at $1.9 \pm 0.6 \text{ Mm}$.

The K_2 emission peaks are on average formed below K_3 , at $0.3\text{--}3.0 \text{ Mm}$. On average, K_{2V} forms at $1.3 \pm 0.5 \text{ Mm}$ and K_{2R} forms at $1.0 \pm 0.5 \text{ Mm}$. Model 2 shows the biggest mean formation heights, 1.4 Mm for K_{2V} and 1.1 Mm for K_{2R} .

The K_{2V} distributions show three maxima in all three models.

The leftmost side maximum at 0.5 Mm is obtained from profiles with a single emission peak. The emission peak is produced in the lower chromosphere by strong downflows following the upward passage of shock waves.

The next peak mode at 0.8 Mm is caused by complex profiles with many emission peaks, where the standard classification cannot be applied.

The principal peak at $1.3\text{--}1.4 \text{ Mm}$ is obtained from standard profiles with two emission peaks. It is strong for K_{2V} and is weak for K_{2R} as the red emission peak is often difficult to measure in normal profiles because it is weak or appears as a slight bump in the line profile but not a local maximum.

Features of the H line are formed below the corresponding features of the K line. On average, H_3 forms 150 km below K_3 , H_{2V} forms 150 km below K_{2V} , and H_{2R} forms 100 km below K_{2R} .

6.2. K_3 minimum

The cores of the K and H lines are the most interesting features as they are the most highly formed parts of the line profiles. At K_3 and H_3 one can observe the middle-upper chromosphere, which is still below the Mg II H and K or H I Ly- α lines in the UV, but above the other visible, infrared triplet of Ca II T, or H I H- α, β lines. Figure 15 illustrates this on the Model 2 slice, that is indicated in Fig. 13.

All strong chromospheric line cores are formed at heights where the magnetic pressure P_B dominates the gas pressure P_{gas} ; this is illustrated by the plasma $\beta = P_{\text{gas}}/P_B = 1$ curve. Owing

to a factor ~ 17 higher opacity, the Mg II H and K lines always form above the Ca II H and K lines. This difference in formation heights goes from 40 to 1900 km depending on the density variation in the atmosphere. At the same time, the H line always forms below the K line, on average 120 km . Both the H and K line cores form around 2200 km in this slice. The 8542 \AA line forms much below, around 1400 km .

At network regions with strong vertical magnetic fields, the transition region lies much lower and the Ca II and Mg II lines are formed very close to each other just below the transition region (for example between a width of 21 and 25 Mm in Fig. 15). In the internetwork magnetic fields are more horizontal and the transition region lies much higher on many density loops, which outline the magnetic field direction. There, the Ca II and the Mg II lines are formed much higher with a much bigger spacing in between their formation heights (for example between a width of $16\text{--}20 \text{ Mm}$). If we define the transition region as the height where the temperature goes above 30 kK , then the K line forms, on average in all three models, 1.25 Mm below the transition region. We did not find any correlation between the K line intensity and the height of the transition region.

We want to illustrate a common feature of strong chromospheric lines. For each model, we composed two images in the XY -plane made of intensities and corresponding formation heights at K_3 given in Fig. 16. In each image there are many white sprinkles in the upper panel and black sprinkles in the lower panel that are caused by misfits of the K_3 feature.

The effect of increasing horizontal resolution is visible from Model 1, which has very diffuse and unsharp structures, to Model 3, which has many small-scale sharp elements. We would like to point attention to the anti-correlation of the observed intensity with the formation height at K_3 . In other words, bright radiation of the network is formed much below dim radiation of the internetwork formed higher up.

Panel a of Fig. 17 shows the validity of the Eddington–Barbier relation at $\mu = 1$ for the K_3 emergent intensity,

$$I(\lambda_3, \mu = 1) = S(\lambda_3, z = z(\tau = 1)), \quad (3)$$

where $\tau = 1$ is at the wavelength position of the K_3 feature.

As the K line is strongly scattering with the photon destruction probability $\epsilon \approx 10^{-4}$ and as CRD is approximately valid at the line core, then the line source function at K_3 is mostly equal to the angle- and profile-averaged intensity \bar{J}^ν . This is correct for $z(\tau = 1) > 1.3 \text{ Mm}$ as can be seen in panel b of Fig. 17. Below $z(\tau = 1) = 1.3 \text{ Mm}$, the line source function becomes more coupled to the local Planck function. The mean intensity of scattered radiation is decreasing with height, which is why we observe an anti-correlation of T_b with $z(\tau = 1)$ in Fig. 16.

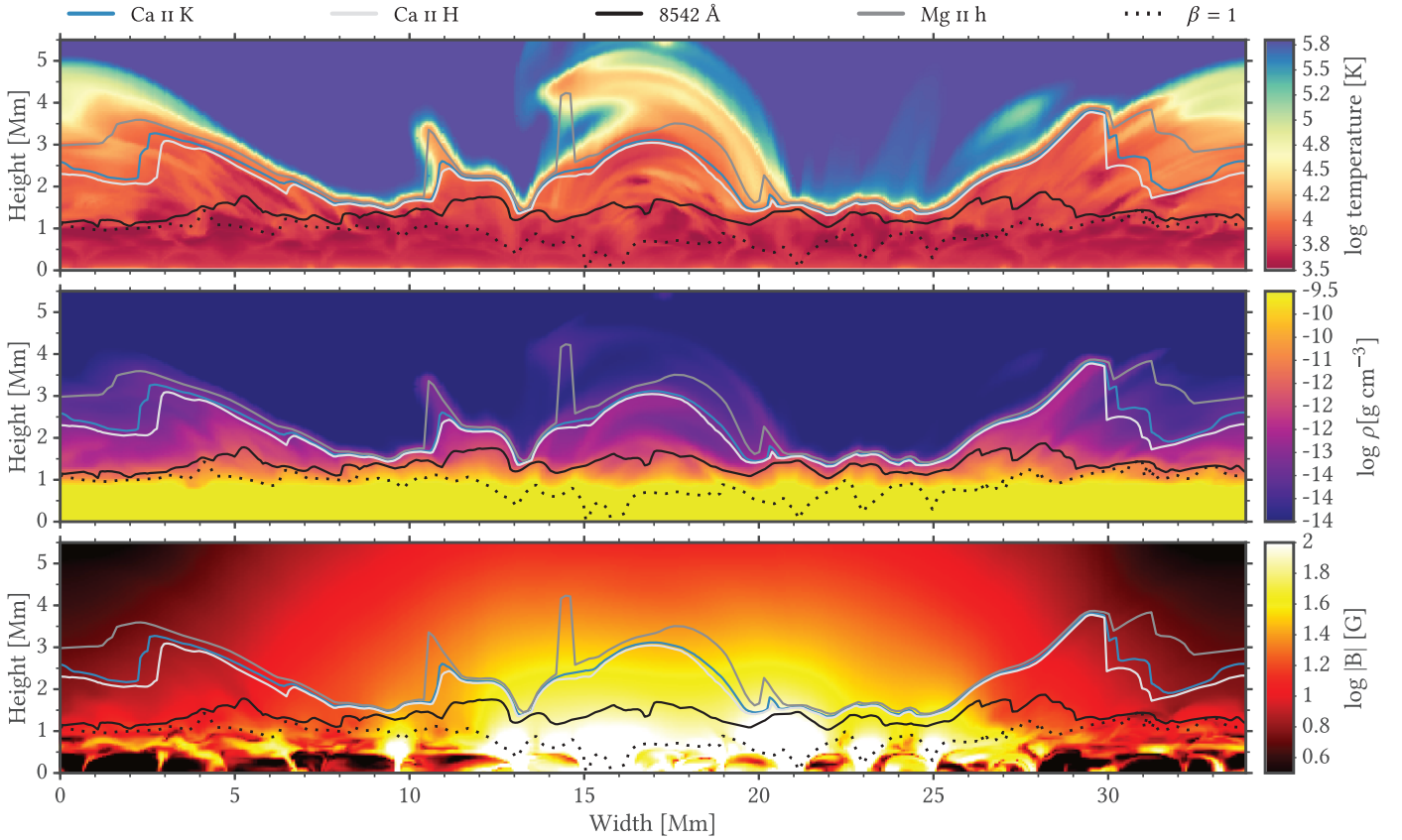


Fig. 15. Maximum formation heights, $\max z(\tau_v = 1)$, of the Ca II K (blue), Ca II H (white), infrared Ca II triplet 8542 Å (black solid), and Mg II h (gray) lines in Model 2, sliced vertically along the main diagonal, where $\max z(\tau_v = 1)$ is taken over all wavelength positions of the respective spectral line profile. The zero point is defined as the average height where the optical depth at 5000 Å is unity. *Upper panel:* gas temperature is indicated. *Middle panel:* mass density is shown. *Lower panel:* magnetic field strength is shown. The plasma β parameter is less than unity above and bigger than unity below the dotted line.

6.3. Diagnostic properties of the H and K lines

Following Leenaarts et al. (2013b) we investigated what kind of diagnostic the H and K lines can provide for the chromosphere. We studied how intensities, wavelength positions, and other derived properties of the vertically emergent ($\mu = 1.00$) synthetic profile features are related to the physical properties of the individual columns of the 3D model atmosphere at the corresponding heights. We present results for the K line only as they are similar for the H line.

We use the following notations. The speed of light is c . The vertical velocity is $v_z(z)$ and it depends on height z . The central wavelength of the K line is λ_0 . For K_{2V} , K_3 , and K_{2R} , we denote their wavelengths $\lambda(K_{2V})$, $\lambda(K_3)$, and $\lambda(K_{2R})$. The same notation in parentheses is used for the emergent intensity I and the corresponding brightness temperature T_b . The formation height of K_3 is $z_3 \equiv z(K_3)$. Similarly, the averaged formation height of K_2 is

$$z_2 = \frac{1}{2}[z_{2V} + z_{2R}] \equiv \frac{1}{2}[z(K_{2V}) + z(K_{2R})]. \quad (4)$$

The Doppler shift of K_3 is

$$v_3 = c \frac{\Delta\lambda_3}{\lambda_0} \equiv c \frac{\lambda_0 - \lambda(K_3)}{\lambda_0}. \quad (5)$$

The averaged Doppler shift of K_2 is

$$v_2 = c \frac{\lambda_0 - \frac{1}{2}[\lambda(K_{2V}) + \lambda(K_{2R})]}{\lambda_0}. \quad (6)$$

The peak-to-peak distance or the peak separation is

$$\Delta v_2 = c \frac{\Delta\lambda_2}{\lambda_0} \equiv c \frac{\lambda(K_{2R}) - \lambda(K_{2V})}{\lambda_0}. \quad (7)$$

The averaged vertical velocity at peaks is

$$\langle v_z \rangle_2 = \frac{1}{2}[v_z(z_{2V}) + v_z(z_{2R})]. \quad (8)$$

The maximum amplitude of the vertical velocity

$$\Delta v_z = \max_{z_2 \leq z \leq z_3} v_z(z) - \min_{z_2 \leq z \leq z_3} v_z(z) \quad (9)$$

is measured between z_2 and z_3 , that is, the range of heights where the central part of the profile between the emission peaks is formed. In the same range of heights we define the mean vertical velocity

$$\langle v_z \rangle_{2-3} = \frac{1}{z_3 - z_2} \int_{z_2}^{z_3} v_z(\zeta) d\zeta. \quad (10)$$

The peak asymmetry A is the same as in Eq. (2).

6.3.1. Velocities

Leenaarts et al. (2013b) showed that the Mg II h and k lines are good for tracing the line-of-sight velocities in the chromosphere through the h_3/k_3 or the h_2/k_2 features. We test whether the same is true for the Ca II H and K lines.

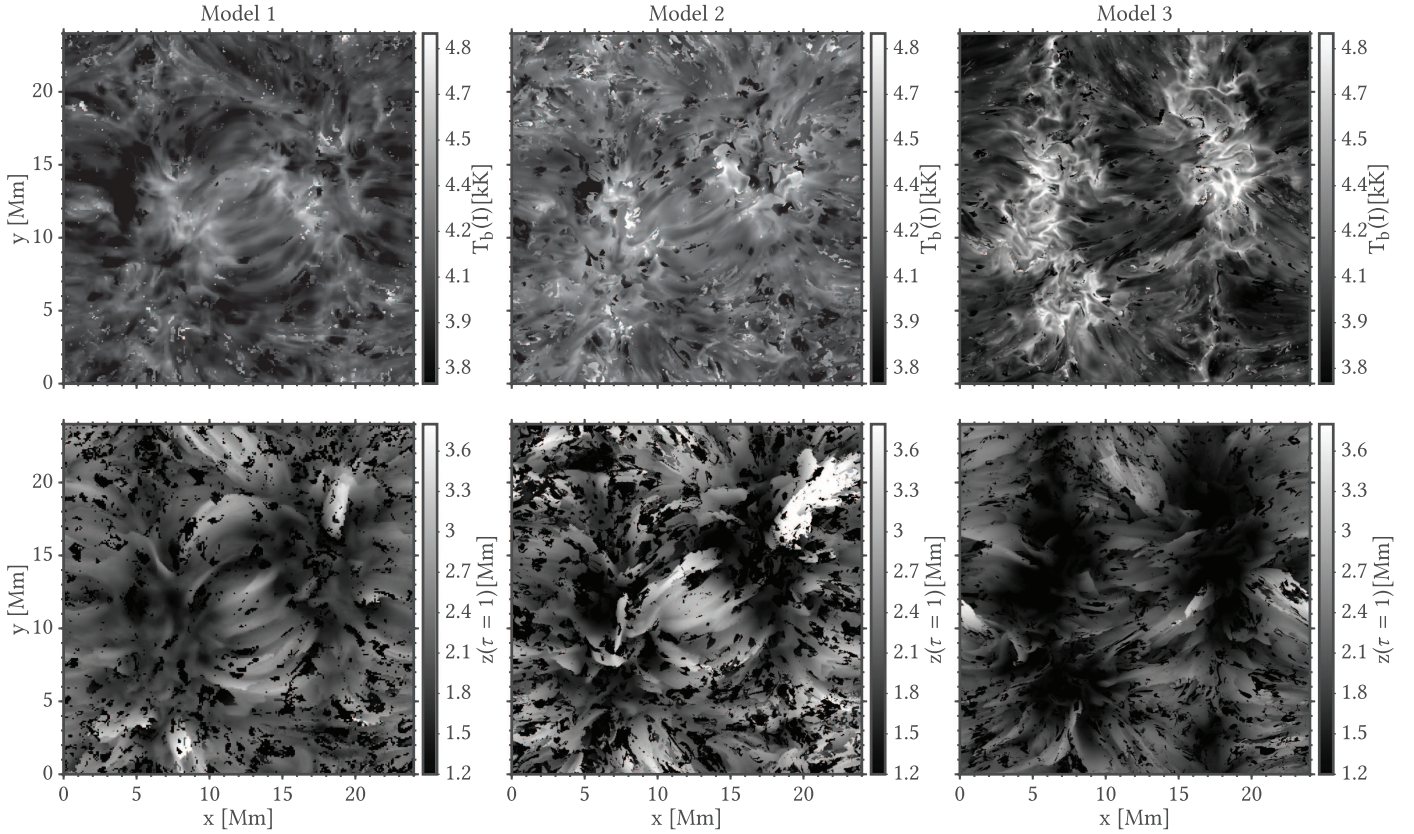


Fig. 16. Emergent intensity expressed as brightness temperature T_b (upper row) and formation height $z(\tau = 1)$ (bottom row) at K_3 for Model 1, 2, and 3 (left, center, and right column) computed at $\mu = 1$.

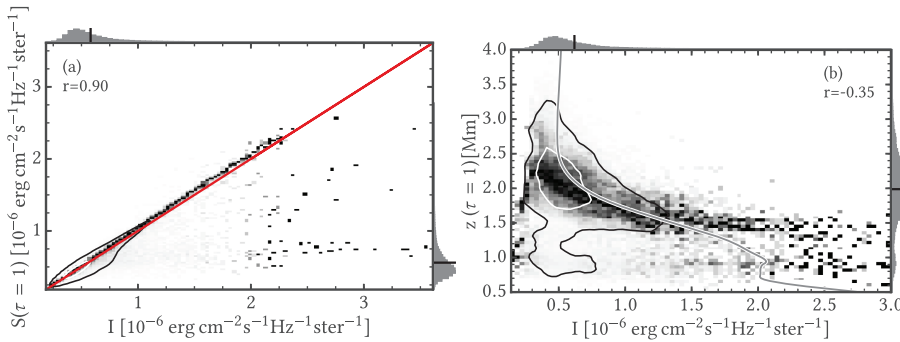


Fig. 17. Formation properties of Ca II K_3 from Model 1. *Panel a:* joint-PDF of the emergent K_3 intensity and the source function at $\tau = 1$ at the wavelength of K_3 are shown. *Panel b:* joint-PDF of the emergent K_3 intensity and the $z(\tau = 1)$ at the wavelength of K_3 are shown. The gray curve in *panel b* shows the horizontally averaged profile-averaged mean intensity \bar{J}^ϕ . The panels follow the same format as Fig. 6.

We examined whether the K_3 Doppler shift v_3 (Eq. (5)) corresponds to the vertical velocity $v_Z(z_3)$ at the K_3 formation height z_3 . Panel a in Fig. 18 shows this is true with a very strong correlation. Two spurious spots outside of the main distribution resulted from K_3 misfits in complex profiles with more than two emission peaks. The wavelength position of K_3 is a very accurate probe for velocities in the upper chromosphere.

We studied how the K_2 peak separation Δv_2 (Eq. (7)) is related to the corresponding maximum amplitude of the vertical velocity Δv_Z (Eq. (9)). Panel b in Fig. 18 shows a decent correlation for $\Delta v_2 < 20 \text{ km s}^{-1}$. An example is given in panel a of Fig. 9, where a 11 km s^{-1} K_2 peak separation corresponds to $\Delta v_Z = 5 \text{ km s}^{-1}$. A larger separation of the K_2 peaks is caused by the deep chromospheric heating discussed in Sect. 6.3.4 and is not dependent on the velocity amplitudes.

We related the averaged K_2 Doppler shift v_2 (Eq. (6)) with the averaged vertical velocity $\langle v_Z \rangle_2$ at K_2 (Eq. (8)). Panel c in Fig. 18 shows that this is a good velocity diagnostic for

the middle chromosphere, especially for strong velocities. The distribution shows a number of points sticking out toward the left at $\langle v_Z \rangle_2 = 0$. These points are mainly caused by misidentifications of one or both of the K_2 peaks. We note that in the simulations one has access to the formation heights of the peaks, while this is not the case for observations. Observationally, v_2 can thus be used to estimate the vertical velocity in the chromosphere at the peak formation heights, but it is not possible to estimate the formation heights themselves.

Finally, we related the peak asymmetry A (Eq. (2)) with the mean vertical velocity $\langle v_Z \rangle_{2-3}$ (Eq. (10)). In the quiet Sun observations, the peak asymmetry is mostly positive indicating in the chromosphere a particular type of downflows that follow upward passages of shock waves (Carlsson & Stein 1997). Panel d in Fig. 18 shows an anti-correlation of A with $\langle v_Z \rangle_{2-3}$, which means that the blue emission peak becomes stronger than the red emission peak if material in the middle–upper chromosphere is mainly moving down and vice versa. This dependence

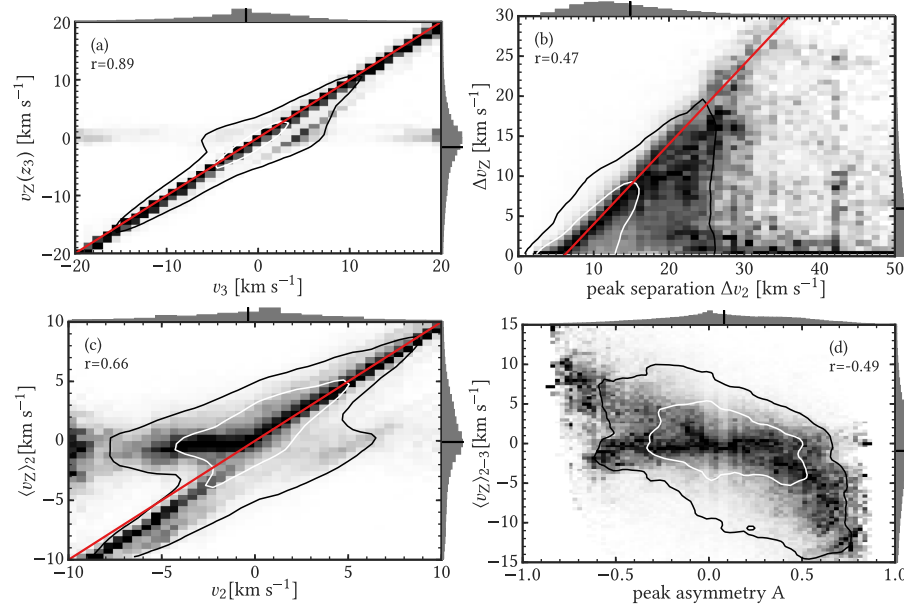


Fig. 18. Correlations of observable K line profile properties for diagnosing vertical velocities in the chromosphere from Model 2. *Panel a:* the K_3 Doppler shift against the vertical velocity at the K_3 formation height is indicated. *Panel b:* the K_2 peak separation against the maximum vertical velocity amplitude between K_2 and K_3 formation heights is shown. *Panel c:* the average K_2 Doppler shift against the averaged vertical velocity at the K_2 formation heights is indicated. *Panel d:* the emission peak asymmetry against the mean vertical velocity between the K_2 and K_3 formation heights is shown. The panels follow the same format as Fig. 6.

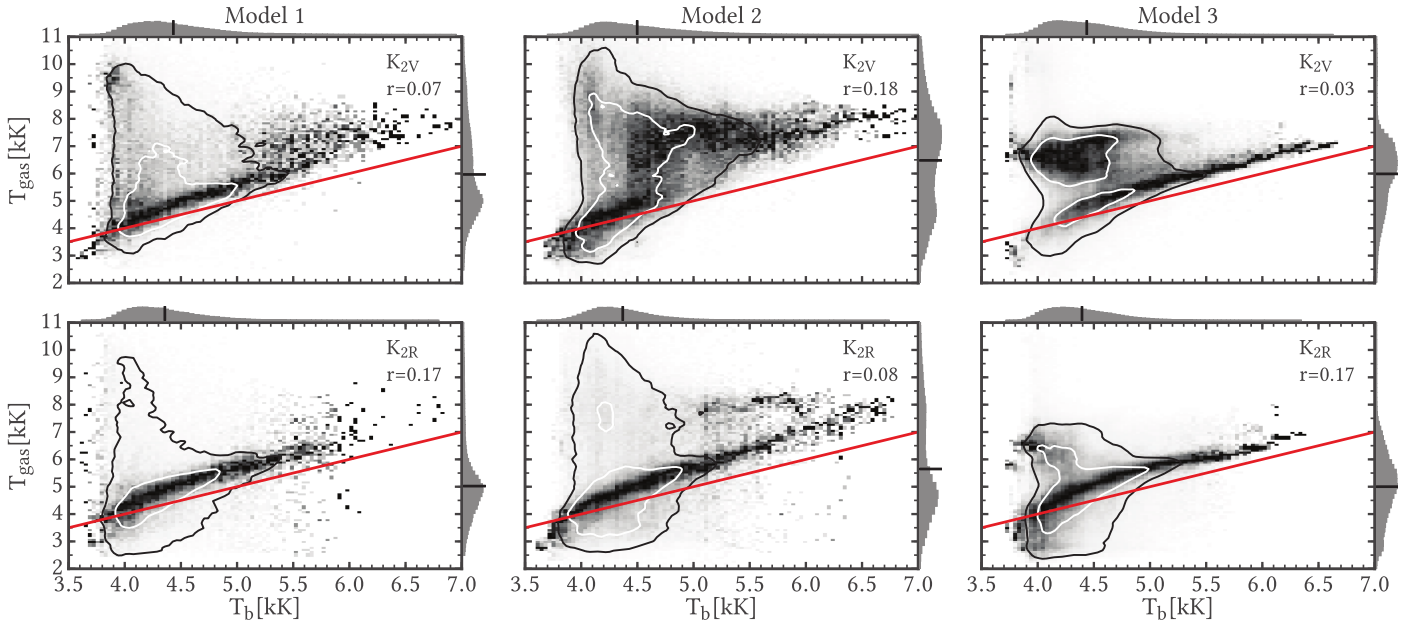


Fig. 19. Calibrations of the observed brightness temperature at K_{2V} (top row) and K_{2R} (bottom row) for measuring the gas temperature at the related formation heights. Results are shown for Models 1, 2, and 3 (left, center, and right column). The panels follow the same format as Fig. 6.

is almost linear for small velocities but then saturates for large velocities.

6.3.2. K_2 intensities

The emission peaks of the H and K lines of Mg II (Leenaarts et al. 2013b) demonstrate a correlation of their brightness temperature T_b with the gas temperature T_{gas} at the corresponding formation heights. We investigated the validity of this relation for the emission peaks of the Ca II H and K lines.

Figure 19 shows correlations between the brightness temperature $T_b(K_{2V})$ at K_{2V} or $T_b(K_{2R})$ at K_{2R} and the related gas temperature $T_{\text{gas}}(z_{2V})$ or $T_{\text{gas}}(z_{2R})$. For each model atmosphere there is a certain range of T_b where this relation is valid, therefore the peaks can probe the gas temperature in the chromosphere.

In Model 1, this range is 4.5–6 kK. Below 4.5 kK, the peak intensity gets set by the scattered radiation in the middle chromosphere and the distribution spreads out decreasing the correlation. Intensities at both peaks underestimate the gas temperature by 0.5–1 kK.

In Model 2, the range of the linear correlation is 4.7–6.8 kK. The blue peak intensity underestimates the gas temperature by ~ 2 kK, while the red peak intensity underestimates it by 1 kK. The difference between red and blue peak is caused by much stronger velocity fields in this model, which causes large variations of the opacity along the line of sight (for examples see Fig. 9).

In Model 3, the validity range is 4.7–6.4 kK. This model shows the most accurate linear dependence with the smallest spread. There are side secondary clusters of points at 3.7–4.6 kK for K_{2V} and at 3.7–4.2 kK for K_{2R} where there is no

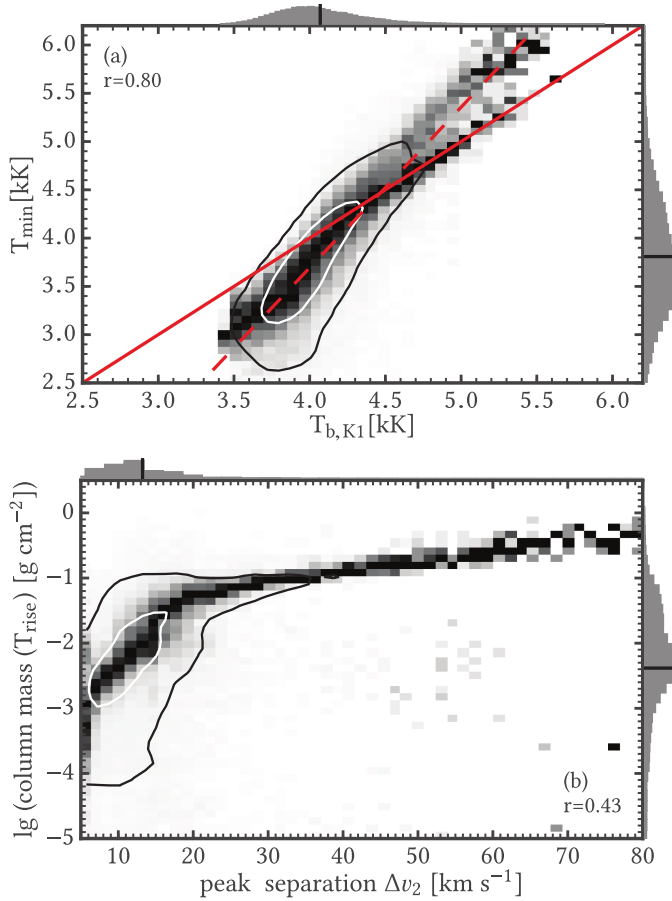


Fig. 20. Observed properties of the lower chromosphere from Model 1. *Panel a:* the averaged brightness temperature at K_1 against the gas temperature at the temperature minimum is shown. The red solid line is $y = x$ and the dashed line is the 3rd-degree polynomial fit. *Panel b:* the K_2 peak separation against the column mass above the temperature rise is shown. The panels follow the same format as Fig. 6.

correlation and intensity is controlled by the scattered radiation.

In all models, the K_{2R} peak shows a stronger correlation than the K_{2V} peak.

We tested the correlations by computing them using the line profiles with a single emission peak only, which constitute only 16% of the entire population. We obtain very similar distributions, therefore we conclude that these types of correlations are not sensitive to our algorithm for the profile feature classification.

We tested this relation for the K_3 feature as well. The line core is strongly scattering and its brightness temperature is not correlated to the local gas temperature. Therefore, the K_3 brightness temperature cannot be used to measure the gas temperature in the chromosphere.

6.3.3. K_1 intensities

The K_1 minima are formed between the upper photosphere and lower chromosphere. There, they are caused by either a global temperature minimum or one of the local minima. The line source function at such heights is often still partially coupled to the Planck function. Therefore the K_1 minima can be used to diagnose the temperature in the temperature minimum.

Shine et al. (1975) investigated how the K_1 intensity relates to the global temperature minimum in the 1D HRSA model atmosphere. These authors found that the brightness temperature at K_1 was lower than the gas temperature at the minimum.

We applied their approach to measure the temperature minimum in our 3D Bifrost model atmospheres. Such 3D R-MHD model atmospheres have a very complicated temperature structure that is not as easy to classify as it can be performed with traditional 1D hydrostatic model atmospheres that typically have a single well-defined temperature minimum around a height of 500 km.

Since the line source function is frequency-dependent in the line wings due to PRD, K_{1V} , or K_{1R} features can be formed at different formation heights. Therefore, we first determine the formation height of each feature and then search in a height interval of 200 km around these formation heights for the deepest temperature minimum. We define the global temperature minimum as the height with the lowest gas temperature obtained either from K_{1V} or K_{1R} .

Panel a in Fig. 20 shows how the averaged brightness temperature $T_b(K_1)$ at K_1 relates to the gas temperature at the minimum. The K_1 brightness temperature overestimates the temperature of the minimum at low K_1 intensities. From $T_b(K_1) = 4.4$ kK and above there are two arms in the distribution. One, along the red solid line, shows a tight linear correlation meaning that the radiation temperature and gas temperature are well coupled. The other, along the red dashed line, underestimates the temperature of the minimum. The atmospheric columns that produce the line along the red solid line all have very wide K_1 separations and formation heights so low in the atmosphere that the source function is still strongly coupled to the Planck function.

In all three models, this global correlation is very strong. We conclude that K_1 could be used to assess the temperature of the temperature minimum using panel a in Fig. 20 as a calibration. The bifurcation of the distribution above $T_b(K_1) = 4.6$ kK adds some ambiguity, however.

6.3.4. K_2 peak separation

As we noted for the distribution on panel b in Fig. 18, there is no correlation between the K_2 peak separation and maximum velocity amplitude in the middle-upper chromosphere if the former is more than 20 km s⁻¹. By applying the Eddington–Barbier approximation, we conjecture that a separation between the K_2 peaks significantly larger than 20 km s⁻¹ indicates that there is a temperature increase that is already much deeper in the atmosphere than is typical for our simulations (an example of a profile is given in panel d of Fig. 9).

We identified the location of this temperature increase assuming that at the formation height z_2 of K_2 the source function is decreasing when moving deeper into the atmosphere. If this is true, we stop at height where the source function is 90% of its value at z_2 . From this height up we integrate the density to obtain the column mass where the temperature rise occurs. If K_2 is misidentified or if the source function is only increasing with increasing depth, we discard this profile from the sample.

Panel b in Fig. 20 shows that K_2 peak separations above 25 km s⁻¹ are indeed associated with a deeply located temperature increase (i.e., at high column mass). The correlation is very tight. We note that in our model atmospheres we only have a very small fraction of profiles that show this effect. Nevertheless, because the effect is based on simple radiation transfer properties we expect that very wide K_2 peak separations can be

evidence of a deep chromospheric temperature rise in observations as well. However, because the observed and simulated line profiles show substantial differences, we also note that observed wide peak separations can be caused by effects not present in our models.

7. Summary and conclusions

We investigated the formation and diagnostic value of the Ca II H and K lines through observations and numerical modeling.

We modeled the Ca II spectrum by considering the non-LTE, 3D RT, and PRD/XRD effects together. 3D RT effects are important in the cores of the lines, while the PRD/XRD effects mostly influence the wings. A joint treatment of all three effects is important to obtain correct synthetic intensities.

We computed synthetic line profiles in 3D non-LTE including XRD from snapshots from three different radiation-MHD models computed with the Bifrost code.

We compared the synthetic spatially averaged spectrum with a standard solar atlas and our SST/CHROMIS observations. None of the model atmospheres reproduces the observed spectral profiles. In Model 2, the emission peaks are usually blended at disk center and become separated only toward the limb. Model 1 and Model 3 reproduce the two emission peaks. All three models have a wavelength separation that is too low between the K_1 and K_2 features. We conclude that something is missing in all models that is responsible for the broader observed profiles. Two possibilities for this are a lack of motions at scales smaller than the photon mean free path (“microturbulence”, 1D modeling shows that amplitudes of 5 km s^{-1} are sufficient), and heating processes that are too weak in the lower chromosphere (see Fig. 8, panel d of Fig. 9, and the lower panel of Fig. 20).

The same behavior has been reported for the h and k lines of Mg II (Leenaarts et al. 2013a,b; Pereira et al. 2013) and C II lines (Rathore & Carlsson 2015) in Model 1. The models also predict a K_2 radiation temperature that is too low.

We compared the center-to-limb variation with Model 1, Model 2, and observations performed at Sacramento Peak (Zirker 1968). The models reproduce the observed trends in variation of the intensity of the line features and the K_1 and K_2 separations, but do not reproduce their absolute values.

We investigated several diagnostic possibilities of the H and K lines. The H_3/K_3 features trace the vertical velocity in the upper chromosphere. Furthermore, the K_2 peak separation correlates with the velocity difference between the K_2 and K_3 formation heights for peak separations below 20 km s^{-1} . For larger peak separation we find a good correlation with the column mass where the chromospheric temperature rise occurs. The K_2 asymmetry can be used to measure the average velocity between the line core and emission peaks.

The model predict a peak separation that is too low and the correlation that we found thus point toward, on average, vertical velocities that are too low and a location of the chromospheric temperature rise in the models that is too high.

The brightness temperature of H_2/K_2 and H_1/K_1 can probe the local conditions in the upper photosphere to the middle chromosphere. We showed that the brightness temperature of H_1/K_1 correlates with the temperature in a local or global temperature minimum along the line of sight. The brightness temperature of the H_2/K_2 features correlates with the gas temperature at their formation heights, especially for high temperatures. The offset between the gas temperature and K_2 brightness temperature is

somewhat different in all three models, which means that the temperature estimates derived from the brightness temperature have an uncertainty in the range of 0.5–2 kK.

The H and K lines of Ca II have similar formation properties similar as the h and k lines of Mg II. The main difference is the larger formation heights of the H and K lines. Within magnetic elements this height difference is small, but in the simulated internetwork regions the difference can be up to 2000 km.

We studied three different model atmospheres that span a large variation of physical conditions, and all models produce similar correlations between observables and the atmospheric parameters. We therefore believe that the correlations presented in this paper will be valid in the quiet Sun. However, these correlations might not be valid under different circumstances, for example in active regions.

The simulations that we use here do not include the Hall term and ambipolar diffusion resulting from the interaction of ions and neutral particles. Martínez-Sykora et al. (2012) has shown that inclusion of those effects in 2.5D models leads to enhanced dissipation of magnetic free energy, which, in turn, leads to an increase in heating in the chromosphere.

In addition, Martínez-Sykora et al. (2017) showed that ion-neutral effects in a different 2.5D simulation with a larger spatial extent and higher spatial resolution, produces structures that have the same properties as type II spicules (De Pontieu et al. 2007). These spicules are notably absent from our simulations and might play a role in setting the average properties of the Ca II H and K line profiles.

All three snapshots that we use are computed with a different equation of state. The equation of state has a large impact on the density and temperature structure in the chromosphere and transition region (Leenaarts et al. 2007; Golding et al. 2016). We therefore cannot draw any conclusions with respect to the effect of EOS or spatial resolution on the line profiles.

Radiative transfer computations as described in this manuscript should be performed on new 3D simulations with a higher resolution, an equation of state including non-equilibrium ionization of both hydrogen and helium, and including the effects of ion-neutral interactions.

Acknowledgements. We thank David Bühler and Jayant Joshi for acquiring the quiet-Sun data. The Swedish 1-m Solar Telescope is operated on the island of La Palma by the Institute for Solar Physics of Stockholm University in the Spanish Observatorio del Roque de los Muchachos of the Instituto de Astrofísica de Canarias. The computations were performed on resources provided by the Swedish National Infrastructure for Computing (SNIC) at the High Performance Computing Center North at Umeå University and the PDC Centre for High Performance Computing (PDC-HPC) at the Royal Institute of Technology in Stockholm. JdlCR is supported by grants from the Swedish Research Council (2015-03994), the Swedish National Space Board (128/15) and the Swedish Civil Contingencies Agency (MSB). This research was supported by the CHROMOBS and CHROMATIC grants of the Knut och Alice Wallenberg foundation and by the Research Council of Norway through the grant “Solar Atmospheric Modelling” and through grants of computing time from the Programme for Supercomputing.

References

- Allende Prieto, C., Lambert, D. L., Hubeny, I., & Lanz, T. 2003, *ApJS*, 147, 363
 Arnaud, M., & Rothenflug, R. 1985, *A&AS*, 60, 425
 Asensio Ramos, A., & de la Cruz Rodríguez, J. 2015, *A&A*, 577, A140
 Asplund, M., Grevesse, N., Sauval, A. J., & Scott, P. 2009, *ARA&A*, 47, 481
 Auer, L. 2003, in *Stellar Atmosphere Modeling*, eds. I. Hubeny, D. Mihalas, & K. Werner, *ASP Conf. Ser.*, 288, 3
 Barklem, P. S., Piskunov, N., & O’Mara, B. J. 2000, *A&AS*, 142, 467
 Bautista, M. A., Romano, P., & Pradhan, A. K. 1998, *ApJS*, 118, 259
 Burgess, A., & Chidichimo, M. C. 1983, *MNRAS*, 203, 1269
 Burgess, A., & Tully, J. A. 1992, *A&A*, 254, 436

- Carlson, B. G. 1963, in *Statistical Physics, Methods in Computational Physics: Advances in Research and Applications*, eds. B. Alder, S. Fernbach, & M. Rotenberg (New York, NY, USA: Academic Press)
- Carlsson, M., & Stein, R. F. 1992, *ApJ*, **397**, L59
- Carlsson, M., & Stein, R. F. 1997, *ApJ*, **481**, 500
- Carlsson, M., Hansteen, V. H., Gudiksen, B. V., Leenaarts, J., & De Pontieu, B. 2016, *A&A*, **585**, A4
- Cauzzi, G., Reardon, K. P., Uitenbroek, H., et al. 2008, *A&A*, **480**, 515
- Cram, L. E., & Dame, L. 1983, *ApJ*, **272**, 355
- Day, R. W. 1974, *Sol. Phys.*, **36**, 25
- de la Cruz Rodríguez, J., Socas-Navarro, H., Carlsson, M., & Leenaarts, J. 2012, *A&A*, **543**, A34
- de la Cruz Rodríguez, J., De Pontieu, B., Carlsson, M., & Rouppe van der Voort, L. H. M. 2013, *ApJ*, **764**, L11
- de la Cruz Rodríguez, J., Löfdahl, M. G., Sütterlin, P., Hillberg, T., & Rouppe van der Voort, L. 2015, *A&A*, **573**, A40
- de la Cruz Rodríguez, J., Leenaarts, J., & Asensio Ramos, A. 2016, *ApJ*, **830**, L30
- De Pontieu, B., McIntosh, S., Hansteen, V. H., et al. 2007, *PASJ*, **59**, 655
- Eddén, B., & Risberg, P. 1956, *Arkiv för Fysik*, **10**, 553
- Engvold, O. 1966, *Astrophys. Nor.*, **10**, 101
- Fontenla, J. M., Avrett, E. H., & Loeser, R. 1993, *ApJ*, **406**, 319
- Golding, T. P., Carlsson, M., & Leenaarts, J. 2014, *ApJ*, **784**, 30
- Golding, T. P., Leenaarts, J., & Carlsson, M. 2016, *ApJ*, **817**, 125
- Grevesse, N., & Swings, J.-P. 1968, *Comptes Rendus Acad. Sci. Paris*, **266**, 110
- Grossmann-Doerth, U., Kneer, F., & Uexküll, M. V. 1974, *Sol. Phys.*, **37**, 85
- Gudiksen, B. V., Carlsson, M., Hansteen, V. H., et al. 2011, *A&A*, **531**, A154
- Hale, G. E., & Ellerman, F. 1904, *ApJ*, **19**, 41
- Henriques, V. M. J. 2012, *A&A*, **548**, A114
- Hubeny, I., & Lites, B. W. 1995, *ApJ*, **455**, 376
- Ibgui, L., Hubeny, I., Lanz, T., & Stehlé, C. 2013, *A&A*, **549**, A126
- Kosugi, T., Matsuzaki, K., Sakao, T., et al. 2007, *Sol. Phys.*, **243**, 3
- Kupka, F., Piskunov, N., Ryabchikova, T. A., Stempels, H. C., & Weiss, W. W. 1999, *A&AS*, **138**, 119
- Lambert, D. L., & Mallia, E. A. 1969, *Sol. Phys.*, **10**, 311
- Lambert, D. L., Mallia, E. A., & Warner, B. 1969, *Sol. Phys.*, **7**, 11
- Leenaarts, J., & Carlsson, M. 2009, in *The Second Hinode Science Meeting: Beyond Discovery – Toward Understanding*, eds. B. Lites, M. Cheung, T. Magara, J. Mariska, & K. Reeves, *ASP Conf. Ser.*, **415**, 87
- Leenaarts, J., & Wedemeyer-Böhm, S. 2005, *A&A*, **431**, 687
- Leenaarts, J., Carlsson, M., Hansteen, V., & Rutten, R. J. 2007, *A&A*, **473**, 625
- Leenaarts, J., Pereira, T. M. D., Carlsson, M., Uitenbroek, H., & De Pontieu, B. 2013a, *ApJ*, **772**, 89
- Leenaarts, J., Pereira, T. M. D., Carlsson, M., Uitenbroek, H., & De Pontieu, B. 2013b, *ApJ*, **772**, 90
- Martínez-Sykora, J., De Pontieu, B., & Hansteen, V. 2012, *ApJ*, **753**, 161
- Martínez-Sykora, J., De Pontieu, B., Hansteen, V. H., et al. 2017, *Science*, **356**, 1269
- Meléndez, M., Bautista, M. A., & Badnell, N. R. 2007, *A&A*, **469**, 1203
- Miyamoto, S. 1953, *Z. Astrophys.*, **31**, 282
- Neckel, H. 1999, *Sol. Phys.*, **184**, 421
- Neckel, H., & Labs, D. 1984, *Sol. Phys.*, **90**, 205
- Olson, G. L., & Kunasz, P. B. 1987, *J. Quant. Spectr. Rad. Transf.*, **38**, 325
- Osterbrock, D. E. 1951, *ApJ*, **114**, 469
- Pereira, T. M. D., Leenaarts, J., De Pontieu, B., Carlsson, M., & Uitenbroek, H. 2013, *ApJ*, **778**, 143
- Pietarila, A., Hirzberger, J., Zakharov, V., & Solanki, S. K. 2009, *A&A*, **502**, 647
- Rezaei, R., Bruls, J. H. M. J., Schmidt, W., et al. 2008, *A&A*, **484**, 503
- 1995, *A&AS*, **112**, 525
- Rathore, B., & Carlsson, M. 2015, *ApJ*, **811**, 80
- Reardon, K. P., Uitenbroek, H., & Cauzzi, G. 2009, *A&A*, **500**, 1239
- Rezaei, R., Bruls, J. H. M. J., Schmidt, W., et al. 2008, *A&A*, **484**, 503
- Rouppe van der Voort, L. H. M. 2002, *A&A*, **389**, 1020
- Rutten, R. J. 2003, *Radiative Transfer in Stellar Atmospheres*, http://www.staff.science.uu.nl/~rutte101/rweb/rjr-edu/coursenotes/rutten_rtsa_notes_2003.pdf
- Rutten, R. J., Hammerschlag, R. H., Bettonvil, F. C. M., Sütterlin, P., & de Wijn, A. G. 2004, *A&A*, **413**, 1183
- Rybicki, G. B., & Hummer, D. G. 1991, *A&A*, **245**, 171
- Rybicki, G. B., & Hummer, D. G. 1992, *A&A*, **262**, 209
- Scharmer, G. B., Bjelksjö, K., Korhonen, T. K., Lindberg, B., & Pettersson, B. 2003, in *Innovative Telescopes and Instrumentation for Solar Astrophysics*, eds. S. L. Keil, & S. V. Avakyan (International Society for Optics and Photonics), *Proc. SPIE*, **4853**, 341
- Scharmer, G. B., Narayan, G., Hillberg, T., et al. 2008, *ApJ*, **689**, L69
- Schorn, R. A., Young, A. T., & Barker, E. S. 1975, *Sol. Phys.*, **43**, 9
- Seaton, M. J., Yan, Y., Mihalas, D., & Pradhan, A. K. 1994, *MNRAS*, **266**, 805
- Sheminova, V. A. 2012, *Sol. Phys.*, **280**, 83
- Shine, R. A., Milkey, R. W., & Mihalas, D. 1975, *ApJ*, **199**, 724
- Shull, J. M., & van Steenberg, M. 1982, *ApJS*, **48**, 95
- Sobotka, M., Dudík, J., Denker, C., et al. 2016, *A&A*, **596**, A1
- Solanki, S. K., Steiner, O., & Uitenbroek, H. 1991, *A&A*, **250**, 220
- Sugar, J., and Corliss, C. 1985, in *Atomic Energy Levels of the Iron-Period Elements: Potassium through Nickel* (Washington, DC: American Chemical Society and the American Institute of Physics for the National Bureau of Standards)
- Sukhorukov, A. V., & Leenaarts, J. 2017, *A&A*, **597**, A46
- Theodosiou, C. E. 1989, *Phys. Rev. A*, **39**, 4880
- Tritschler, A., Schmidt, W., Uitenbroek, H., & Wedemeyer-Böhm, S. 2007, *A&A*, **462**, 303
- Uitenbroek, H. 1989, *A&A*, **213**, 360
- Uitenbroek, H. 2001, *ApJ*, **557**, 389
- Vardavas, I. M., & Cram, L. E. 1974, *Sol. Phys.*, **38**, 367
- Zirin, H. 1974, *Sol. Phys.*, **38**, 91
- Zirker, J. B. 1968, *Sol. Phys.*, **3**, 164